Enzyme-Responsive Intracellular Controlled Release Using Nanometric Silica Mesoporous Supports Capped with "Saccharides"

Andrea Bernardos,[†,‡,⊥] Laura Mondragón,[†,‡,§] Elena Aznar,[†,‡,§] M. Dolores Marcos,[†,‡,§] Ramón Martínez-Máñez,[†,‡,§,*] Félix Sancenón,[†,‡,§] Juan Soto,[†,‡] José Manuel Barat,[⊥] Enrique Pérez-Payá,[¶,#] Carmen Guillem,[▽] and Pedro Amorós[▽]

[†]Instituto de Reconocimiento Molecular y Desarrollo Tecnológico (IDM), Centro Mixto Universidad Politécnica de Valencia—Universidad de Valencia, Spain, [‡]Departamento de Química, Universidad Politécnica de Valencia, Camino de Vera s/n, E-46022, Valencia, Spain, [§]CIBER de Bioingeniería, Biomateriales y Nanomedicina (CIBER-BBN), [⊥]Grupo de Investigación e Innovación Alimentaria (CUINA), [¶]Centro de Investigación Príncipe Felipe, Laboratorio Péptidos y Proteínas, Avda. Autopista al Saler, 16, E-46012 Valencia, Spain, [#]IBV-CSIC, Jaime Roig, 11, E-46010, Valencia, Spain, and [▽]Institut de Ciència dels Materials (ICMUV), Universitat de Valencia, P.O. Box 2085, E-46071 Valencia, Spain

ABSTRACT The synthesis of new capped silica mesoporous nanoparticles for on-command delivery applications is described. The gate-like functional hybrid systems consisted of nanoscopic MCM-41-based materials functionalized on the pore outlets with different "saccharide" derivatives and a dye contained in the mesopores. A series of hydrolyzed starch products as saccharides were selected. The mesoporous silica nanoparticles S1, S2, and S3 containing the grafted starch derivatives Glucidex 47, Gludicex 39, and Glucidex 29 were synthesized. Additionally, for comparative purposes solid S4 containing lactose was prepared. Delivery studies in pure water in the presence of pancreatin or β-D-galactosidase were carried out for S1—S3 and S4, respectively. S1, S2, and especially S3 showed very low release in the absence of enzyme, but displayed cargo delivery in the presence of the corresponding enzyme. Moreover, nanoparticles of S1 were used to study the controlled release of the dye in intracellular media. Cell viability assays using HeLa and LLC-PK1 cells indicated that S1 nanoparticles were devoid of unspecific cell toxicity. The endocytosis process for S1 nanoparticle internalization in HeLa cells was confirmed, and the anchored starch was degraded by the lysosomal enzymes. Furthermore, a new mesoporous silica nanoparticle functionalized with Glucidex 47 and loaded with a cytotoxic, S1-DOX, was developed. The cell viability with S1-DOX decreased due to the internalization of the nanoparticle, enzyme-dependent opening of the saccharide molecular gate and the consequent release of the cytotoxic agent. As far as the authors know, this is the first example of enzyme-induced in-cell delivery using capped silica mesoporous nanoparticles.

KEYWORDS: carbohydrates · enzyme · intracellular controlled release · mesoporous · gate

Controlled release of therapeutic drugs, peptides, or nucleic acid fragments in a specific cell is a new and promising research field in biomedical sciences. Traditional delivery systems are in most cases based on polymers that usually release their cargo *via* diffusion-controlled processes or through degradation of the polymer container.[1−7] In recent years, as an alternative to polymeric materials, silica mesoporous supports (SMPS) have been used as inorganic scaffolds for the storage and release of drugs and organic molecules.[8−10] Silica mesoporous supports provide unique features such as stability, biocompatibility, large load capacity, and the possibility to include gate-like scaffoldings on the external surface for the design of nanodevices for on-command delivery applications.[11−16] Most of the gated stimuli-responsive systems are based on biochannels and biogates that utilize movable mechanisms triggered by specific stimuli. SMPS-based systems with control release properties have been reported. Such systems, containing different gate-like scaffoldings, are sensitive to changes in the media pH or redox conditions as well as to light as triggers for uncapping the pores.[17−19]

The first gated SMPS was developed by Fujiwara *et al.*[20,21] *via* reversible photodimerization of coumarin attached to the pore outlets that were sensitive to light. Since then, other photochemical gated systems based on cis−trans isomerization of azobenzene moieties,[22−25] the association and light-operated dissociation of a α-cyclodextrin with azobenzene groups,[26−28] and the spiropyran−merocynine photoswitchable transformation[29] have been reported. pH is also a widely used stimulus for the control of mass transport in mesoporous materials. The authors recently reported the first gated hybrid system, using SMPS functionalized with polyamines on the external surface, operating in an aqueous solution under pH and anion control.[30−32] Additional systems

*Address correspondence to rmaez@qim.upv.es.

Received for review February 22, 2010 and accepted October 01, 2010.

Published online October 19, 2010.
10.1021/nn101499d

involving carboxylates[33] pseudorotaxanes,[34−37] inclusion complexes with cucurbit[6]uril,[38−40] cucurbit[7]uril,[41] and α-cyclodextrins[42] have also been prepared. Furthermore dual pH- and photoswitched release of guests has been achieved in SMPS capped with boronic acid-functionalized gold nanoparticles.[43] Changes in the media redox conditions are another popular approach to control delivery in capped mesoporous materials. Lin *et al.* developed capped materials using mesoporous scaffoldings capped with CdS, gold, or magnetic nanoparticles attached to the SMPS through disulfide linkages that were broken up upon addition of certain reducing compounds.[44−54] Also, the rupture of disulfide linkages in molecular-based systems[55] and polymeric networks has been used for on-command delivery.[56,57] Zink and Stoddart prepared several gated materials triggered by redox inputs that were equipped with nanovalves based on rotaxanes and pseudorotaxanes containing redox active moieties.[58−62] Apart from the examples described above, which use redox-, light-, and pH-triggered systems, some additional exploratory studies that use alternative external stimuli such as temperature[63] and the presence of certain anions[64] have also been reported. Another use of these hybrid gated nanomaterials deals with the development of new signaling protocols. The release of an entrapped dye triggered by a specific guest is used in this paradigm which leads to the development of novel hybrid sensing materials showing enhanced signaling features.[65−67]

Although some efforts have been made to prepare SMPS containing different gate-like scaffoldings, the development of real systems for controlled release is still in its incipient stage. For instance, some of the reported systems display gating features in nonaqueous solvents, employ gate-like scaffoldings that require large synthetic efforts, or use external stimuli that are difficult to apply to certain delivery applications. In addition, there is an almost complete lack of SMPS-based systems showing a selective delivery induced by target biomolecules. One of the few examples involves the use of antibody-capped mesoporous nanocontainers that are specifically uncapped in the presence of the corresponding antigen.[68] The enzyme−substrate system can also offer opportunities for the design of sensitive and specific SMPS-based nanodevices. In a first proof-of-the-concept Zink *et al.* functionalized the external surface of SMPS with a [2]rotaxane capped with an ester-linked adamantyl stopper.[69,70] The functionalized SMPS device showed "zero release" until the addition of porcine liver esterase (PLE) which induced dethreading of the [2]rotaxane due to hydrolysis of the adamantyl ester. More recently, Bein *et al.* have attached avidin caps on biotinylated SMPS.[71] The avidin−biotin complex formation resulted in a tight closure of the pores. Addition of the protease trypsin resulted in the hydrolysis of the attached protein avidin and the release of the entrapped guest. The authors have contributed to the field reporting mesoporous silica supports capped with lactose which were selectively uncapped in the presence of enzyme β-D-galactosidase.[72] Also, Kim *et al.* reported the preparation of silica nanoparticles functionalized through a click chemistry reaction, with β-cyclodextrin as gatekeepers.[73] The addition of α-amylase induced the release of calcein due to hydrolysis of the cyclodextrin core.

The groundwork done suggests that enzymatic degradation of capped scaffoldings in SMPS is a suitable protocol for the on-command delivery of entrapped substances. In fact, the possibility of using enzymes for selective release applications opens a wide range of new perspectives in the development of biocompatible delivery systems using silica mesoporous supports. However, as far as the authors know, examples of enzyme-induced delivery in living cells using capped silica mesoporous nanoparticles have not yet been reported. As a continuation of the authors' previous work in this field, the synthesis, characterization, and controlled release experiments using nanometric SMPS functionalized with "saccharides" are reported herein. Delivery processes in the presence of enzymes are studied and the internalization of saccharide-capped nanoparticles in cells is also demonstrated.

RESULTS AND DISCUSSION

The Gated Materials. The incorporation of gate-like ensembles on mesoporous scaffoldings has proven to be a suitable approach for the development of nanoscopic solids for mass transport and controlled release applications. As stated in the introduction section, most of the gated materials developed make use of molecular/supramolecular interactions for the fine control of cargo delivery. Very few examples use biomolecules for capping or uncapping protocols. Following the authors' interest in the application of biological interactions, as triggered control for delivery, attention here was centered on the use of enzymes as "biological-keys".

Scheme 1 shows the proposed paradigm for the preparation of the gated material. In this approach, MCM-41 was used as an inorganic scaffold in the form of nanoparticles (*vide infra*). The MCM-41 support contains mesopores in the 2−3 nm range that allow the encapsulation of certain guests. The aim was to design biocompatible, easy-to-prepare, and low-cost capping systems in order to synthesize simple gated-scaffoldings to be used efficiently in delivery applications. Among different possibilities, attention was focused on the use of saccharides. With this goal in mind, and at the same time seeking to avoid complex synthetic routes to saccharide derivatives, the use of commercially available hydrolyzed starch products was opted for.[74] Hydrolyzed starch is obtained by the moderate hydrolysis of starch. The degree of starch hydrolysis is indicated by the dextrose equivalent (DE)[75] which denotes the percentage fraction of reducing sug-

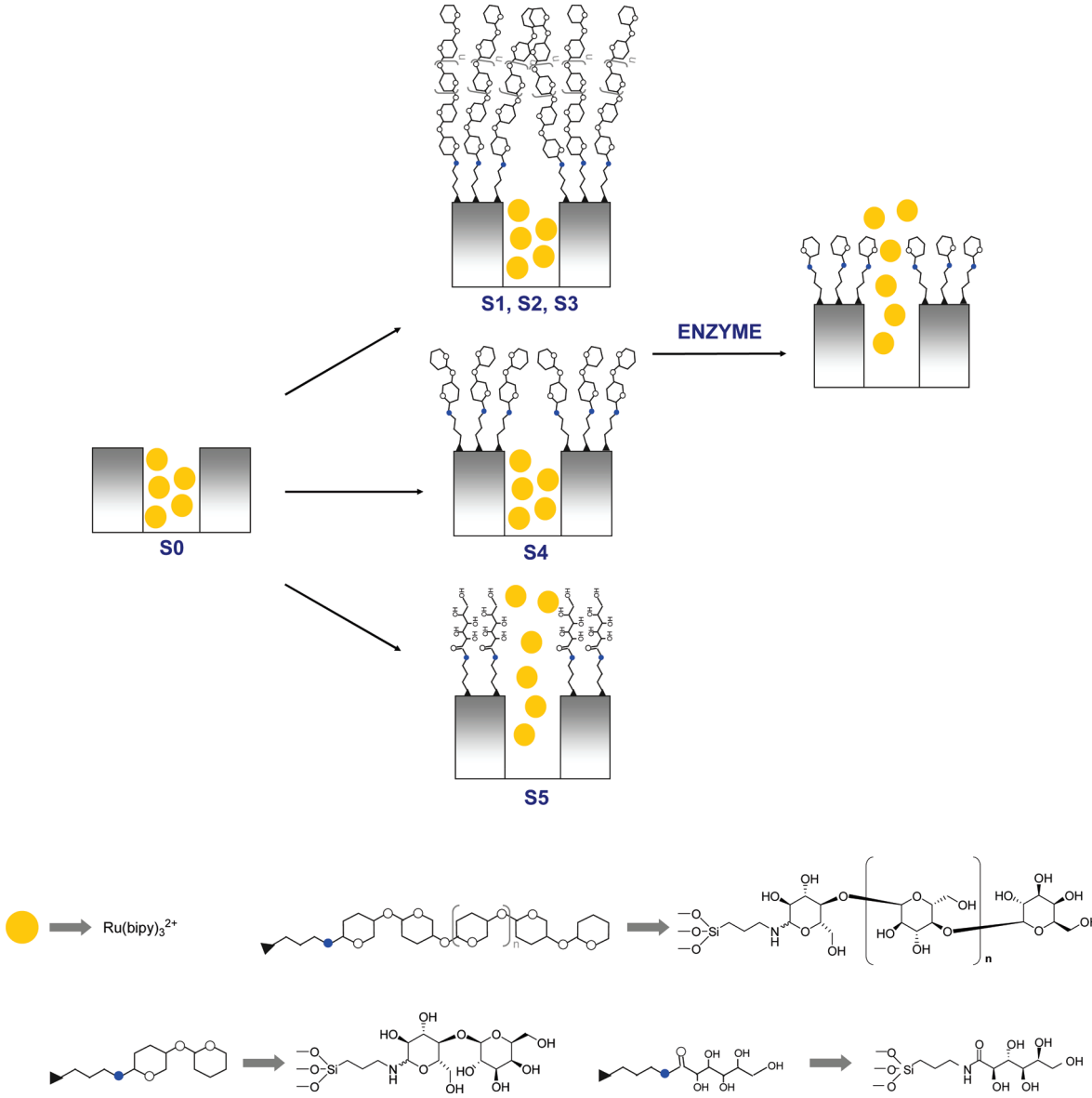

Scheme 1. Schematic representation of the synthesis of hybrid mesoporous nanoparticles S1−S4 capped with trialkoxysilane carbohydrate derivatives and S5 functionalized with *N*-(3-triethoxysilylpropyl)gluconamide. Addition of enzymes to S1−S4 solids would uncap the mesopores *via* the selective hydrolysis of the saccharides anchored on the mesoporous external surface.

ars in the sample (DE 1 is equivalent to nonhydrolyzed starch whereas DE 100 is equivalent to glucose). For this work the following dextrose equivalents (DE) were used; Glucidex 47 (5% glucose, 50% maltose, 45% oligosaccharides and polysaccharides), Glucidex 39 (3% glucose, 37% maltose, 60% oligosaccharides and polysaccharides) and Glucidex 29 (10% glucose, 9% maltose, 81% oligosaccharides and polysaccharides). Additionally, for comparative purposes, lactose[76] was also used as a capping molecule. Carbohydrate polymers and mixtures of carbohydrate polymers are readily available simple saccharides that have been widely used as food additives and biodegradable systems and matrices for the stabilization of certain species.[77]

The hydrolyzed starch derivatives (Glucidex 47, 39, and 29) were reacted with 3-aminopropyltriethoxysilane in ethanol to yield the corresponding alkoxysilane derivatives (**1**, **2**, **3**) (see Scheme 2), whereas the capping molecule **4** was prepared *via* reaction of 3-aminopropyltriethoxysilane with lactose (see Scheme 2).[78] The further anchoring of these silane derivatives **1**, **2**, **3**, and **4** on the external surface of the SMPS resulted in the preparation of solids **S1**, **S2**, **S3**, and **S4**. The anchoring of these saccharide derivatives were expected to inhibit cargo delivery due to the formation, around the pore outlets, of a dense hydrogen-bonding, interaction-based, saccharide network. The working hypothesis predicts that in the presence of pancreatin (containing amylases able to hydrolyze the 1→4 glycosidic bond between β-D-glucoses present in the starch) or β-D-galactosidase (able to hydrolyze 1→4 glycosidic bond between β-D-galactose and β-D-glucose in lactose) the hydrolysis of the saccharide network results in an uncapping of the pores in **S1**−**S3** and **S4**, respectively, allowing delivery of the en-

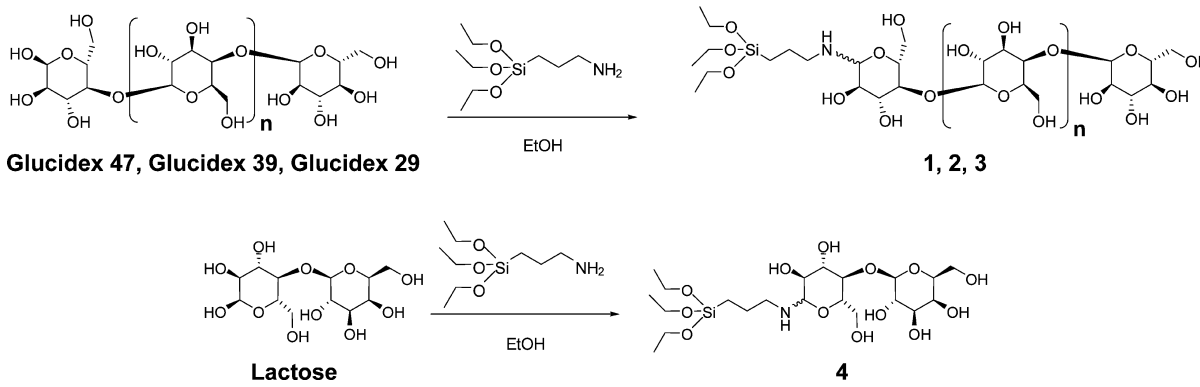

Scheme 2. Synthesis of trialkoxysilane hydrolyzed starch derivatives 1, 2, and 3, and synthesis of trialkoxysilane lactose derivative 4.

trapped molecule (*vide infra*). $[Ru(bipy)_3]^{2+}$ was selected as a guest for delivery. The delivery of the ruthenium complex from the pore voids to the aqueous solution (the uncapping protocol) can be easy followed *via* monitoring of the absorption band at 453 nm in the aqueous phase.

The final solids (**S1**, **S2**, **S3**, and **S4**) must ideally contain the oligosaccharide derivative anchored to the external surface, whereas the dye must be contained in the mesoporous channels. To prepare the final hybrid materials with these requirements a previously reported two-step synthetic procedure was used. In the first step, the mesoporous nanoparticles were added to a solution containing a high concentration of $[Ru(bipy)_3]^{2+}$ dye in order to achieve an efficient loading of the pores. Then, in the same mixture (second step of the material preparation) the hydrolyzed starch derivatized with trialkoxysilane moieties **1** (from Glucidex 47), **2** (from Glucidex 39), **3** (from Glucidex 29), or the lactose derivative **4** was added to the suspensions. This would lead to hybrid materials in which the saccharides are basically placed on the external surface of the mesoporous support, bearing in mind that the anchoring of the corresponding saccharide is carried out when the mesopores are filled with the dye. Finally the yellow/orange solids (**S1**, **S2**, **S3**, and **S4**) were filtered, washed with water, and dried at 40 °C for 12 h. As appropriate controls, solids **S0**, **S5**, and **S6** were prepared. Solid **S0** is an SMPS with $[Ru(bipy)_3]^{2+}$ dye filling the pores but lacking any further functionalization on the surface. Solid **S5** contains the $[Ru(bipy)_3]^{2+}$ dye in the pores and was additionally functionalized on the surface with the commercially available *N*-(3-triethoxysilylpropyl)gluconamide derivative (see Scheme 1). This solid, functionalized with a monosaccharide (a glucose derivative), assesses the degree of effect, if any, that the hydrolyzed starch (**1**, **2**, and **3**) and the disaccharide lactose (**4**) grafted on the pore outlets have on the dye delivery from solids **S1**−**S4** in the presence of suitable enzymes. Solid **S6** is SMPS without any dye in the interior of the pores and functionalized with the hydrolyzed starch derivative **1** (from Glucidex 47). This solid was prepared exactly according to the surface functionalization procedures used.

Characterization of the Solids. The solids prepared were characterized using standard techniques. Figure 1 shows powder X-ray patterns of the solids MCM-41 as-synthesized, MCM-41 calcined, and **S1**, **S2**, **S3**, and **S6**. The XRD of siliceous MCM-41 as-synthesized (curve a) shows the typical four low-angle reflections of a hexagonal ordered array indexed as (100), (110), (200), and (210) Bragg peaks. From the XRD data an a_0 cell parameter of 46.43 Å (d_{100} spacing of 40.21 Å) was calculated. In curve b, corresponding to the MCM-41 calcined sample, a significant shift of the (100) reflection in the XRD is clearly observed. This displacement, together with the broadening of the (110) and (200) reflections,

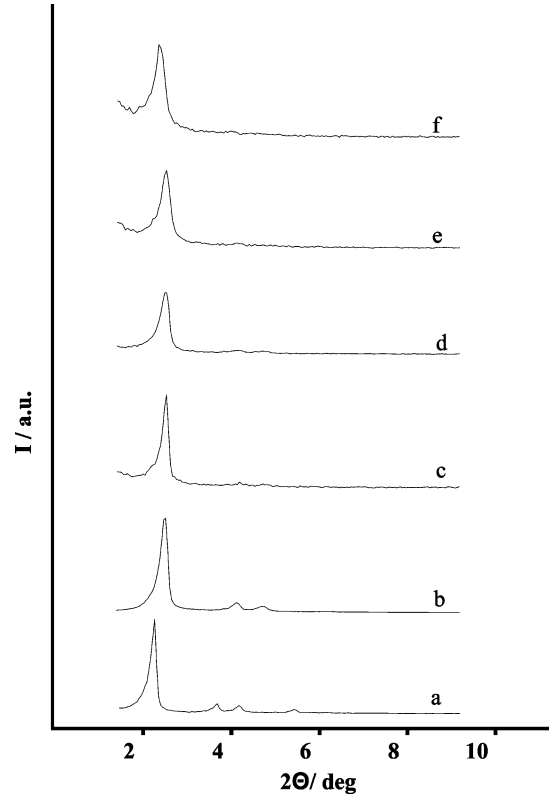

Figure 1. X-ray pattern of (a) MCM-41 as-synthesized, (b) MCM-41 calcined, (c) S1, (d) S2, (e) S3, and (f) S6.

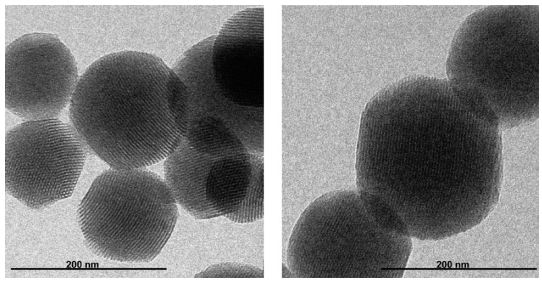

Figure 2. TEM image of MCM-41 calcined (a) and solid S3 (b) showing the typical porosity of the MCM-41 matrix.

is consistent with an approximate cell contraction of *ca.* 6−8 Å and attributed to the condensation of silanols during the calcination step. Figure 1 also shows the XRD patterns for solids **S1**, **S2**, **S3**, and **S6** (curves c, d, e, and f, respectively). For these materials, the reflections (110) and (200) are lost, most likely due to a reduction of contrast as consequence of the functionalization process. Nevertheless, the presence of the d_{100} peak in the XRD patterns in all cases indicated that the process of pore loading with the $[Ru(bipy)_3]^{2+}$ complex, and the additional functionalization with the corresponding saccharides, did not to a large extent modify the mesoporous MCM-41 scaffolding. **S4** and **S5** show XRD profiles similar to those from **S1**−**S3** (not shown). The presence in the final functionalized solids of the mesoporous structure was also confirmed from the TEM analysis, in which the typical channels of the MCM-41 matrix are visualized as alternate black and white stripes (see Figure 2 for MCM-41 calcined (a) and solid **S3** (b)). The figure also shows that the prepared MCM-41-based materials are obtained as spherical particles with diameters ranging from 100 to 200 nm.

The N_2 adsorption−desorption isotherms of the nanoparticulated MCM-41 calcined material is shown in Figure 3 A typical curve for these mesoporous solids consisting of an adsorption step at intermediate P/P_0 value (0.1−0.3) can be observed. This curve corresponds to a type IV isotherm, in which the observed step deals with nitrogen condensation inside the mesopores. The absence of a hysteresis loop in this interval and the narrow BJH pore distribution suggest the existence of uniform cylindrical mesopores (pore diameter of 2.29 nm and pore volume of 0.62 $cm^3\ g^{-1}$ calculated by using the BJH model on the adsorption branch of the isotherm). The application of the BET model resulted in a value of 975 m^2/g for the total specific surface. From the XRD, porosimetry and TEM studies, the a_0 cell parameter (3.98 nm), the pore diameter (2.29 nm), and a value for the wall thickness of 1.69 nm were calculated. In addition to this adsorption step associated to the micelle generated mesopores, a second feature appears in the isotherm at a high relative pressure ($P/P_0 > 0.8$). This adsorption corresponds to the filling of the large voids among the particles (0.48 $cm^3\ g^{-1}$ calculated by using the BJH model) and therefore must be

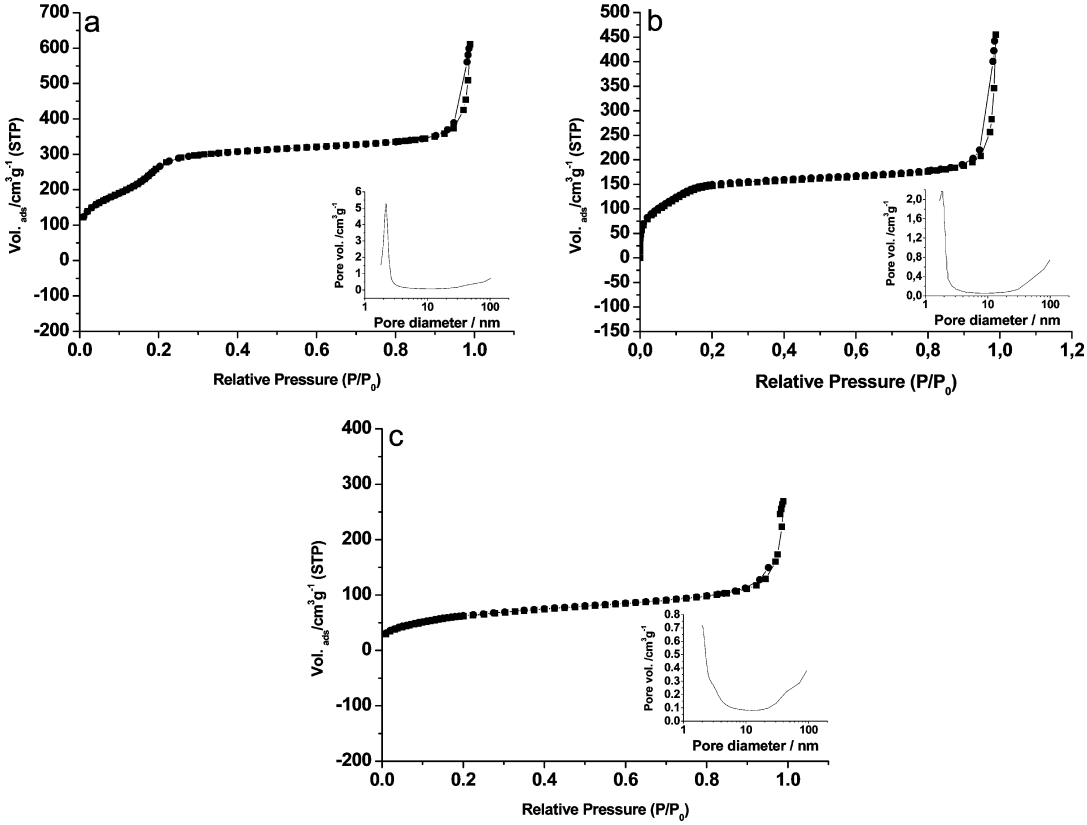

Figure 3. Nitrogen adsorption−desorption isotherms for (a) MCM-41 mesoporous material, (b) S6, and (c) S1 materials. Insets: Pore size distribution of each material.

considered as a textural-like porosity. In this case, the curves show a characteristic H1 hysteresis loop and a wide pore-size distribution.

The N_2 adsorption−desorption isotherm of **S1** is typical of mesoporous systems with practically filled mesopores (see Figure 3c). Consequently, relatively low N_2 adsorbed volume (BJH mesopore volume = 0.13 $cm^3\ g^{-1}$) and surface area (231 m^2/g) values were calculated. In fact, this solid shows flat curves when compared (at the same scale) to those of the MCM-41 parent material and the **S6** solid without dye, this indicates significant pore blocking and the subsequent absence of appreciable mesoporosity. Despite the significant pore volume decrease, some features can still be observed in the BJH mesopore size distribution such as a maximum at 1.8 nm (on the border between meso and micropores) and several shoulders in the 2−3 nm range. Additionally, the textural porosity is preserved and only a certain decrease (0.31 $cm^3\ g^{-1}$) when compared to the parent silica is observed. **S2**, **S3**, **S4**, and **S5** samples show similar N_2 adsorption−desorption isotherms to that shown by **S1**. This is an expected result bearing in mind that all the solids have dye molecules sited at the pores and assuming a certain collapse of the saccharide groups anchored to the pore entrances, while taking into account the dry conditions achieved during the sample evacuation prior to the analysis (*vide infra*). Similar results have been observed by the authors in related systems.

An intermediate behavior between those of nanoparticulated MCM-41 and functionalized and dye charged samples (**S1**, **S2**, **S3**, **S4**, and **S5**) is observed for **S6**. Although the N_2 adsorption−desorption isotherm of **S6** (see Figure 3b) is qualitatively similar to the isotherm of MCM-41 (the two well-defined adsorption steps ascribed to the mesopores and the textural pores are preserved) an appreciable decrease both in the N_2 volume adsorbed (BJH mesopore volume = 0.28 $cm^3\ g^{-1}$) and surface area (567 m^2/g) was measured as expected. The area of solid **S6** was reduced *ca.* 40%, when compared to that presented by MCM-41, due to the external grafting of derivative **1**. On the other hand, the difference between **S1** and **S6** isotherms is clearly related to the filled or empty (with the ruthenium dye complex) nature of the mesopores, respectively. Therefore, for a similar functionalization degree with saccharides, the higher surface area and pore volume for **S6** must be due to the absence of the dye in the interior of the mesopores. Application of the BJH model leads to an average pore diameter of 2.16 nm. As observed for **S1**, the BJH pore size distribution shows a maximum at 1.85 nm (on the border between meso- and micropores) and several shoulders. The presence or absence of dye inside the mesopores does not affect the textural-like porosity. In fact, the second adsorption step at high relative pressure ($P/P_0 > 0.8$) which appears in the isotherm of **S6** and similar BJH textural pore volumes can be estimated for **S1** (0.31 $cm^3\ g^{-1}$) and **S6** (0.30 $cm^3\ g^{-1}$). These data support the fact that the dye molecules are specifically incorporated inside the ordered mesopores. BET specific surface values, pore volumes, and pore sizes calculated from the N_2 adsorption−desorption isotherms for MCM-41, **S1**, **S2**, **S3**, **S4**, **S5**, and **S6** are listed in Table 1.

TABLE 1. BET Specific Surface Values, Pore Volumes and Pore Sizes Calculated from the N_2 Adsorption−Desorption Isotherms for Selected Materials

	S_{BET} ($m^2\ g^{-1}$)	pore volume[a] ($cm^3\ g^{-1}$)	pore size [a,b] (nm)
MCM-41 (nanoparticle)	975	0.62	2.29
S1	231	0.13	2.46
S2	804	0.49	2.44
S3	193	0.09	2.29
S4	45	0.04	2.30
S5	10	0.01	2.20
S6	567	0.28	2.16

[a]Pore volumes and pore sizes are only associated with intraparticle mesopores. [b]Pore size estimated by using the BJH model applied on the adsorption branch of the isotherm.

Considered as a whole, the N_2 adsorption−desorption data illustrate the effective pore blocking that occurs when the saccharide functional groups outside the pore and the dyes inside the mesopores are present in a cooperative way. Moreover, as previously described for related gate-like ensembles, the dry conditions required for sample preparation previous to the adsorption experiments must favor a certain saccharide dehydration with the subsequent collapse on the external surface. This collapse would block the mesopores to a large extent. In the absence of dye molecules inside the mesopores, a slightly higher porosity seems to be accessible for nitrogen. This last behavior is a direct consequence of the evolution of large complexes occupying the mesoporous voids. This loss of the cooperative blocking effect favors a certain increase of the internal empty volume. In all materials containing dye molecules and functional groups, similar pore sizes and volume values were measured. The BJH pore size distributions of these last materials (**S1**, **S2**, **S3**, **S4**, and **S5**) show maximum peaks and/or appreciable shoulders at pore sizes around 1.8−2.0 nm. These values (lower than those calculated for the pure silica parent material), seem to be more realistic than those estimated by the application of the BJH model. The decrease in mesopore size to the range of supermicropores could be viewed as a noncompletely efficient collapse of the functional arms on the mesopore entrances and even to a certain inhomogeneity in the density of functionalized saccharides.

The contents of saccharides and dye in solids **S0**, **S1**, **S2**, **S3**, **S4**, **S5**, and **S6** were determined by elemental and thermogravimetric analysis and are shown in Table 2. Solids **S1**, **S2**, and **S3** functionalized on the

TABLE 2. Content (α) in Grams of Saccharide and Dye per Gram of SiO_2 for Solids S0, S1, S2, S3, S4, S5 and S6

solid	$\alpha_{saccharide}$ (g/g SiO_2)	α_{dye} (g/g SiO_2)
S0		0.112
S1	0.067	0.099
S2	0.073	0.085
S3	0.055	0.090
S4	0.114	0.064
S5	0.068	0.257
S6	0.124	

outer surface with hydrolyzed starch showed very similar contents that range from 0.055 to 0.073 g/g for the polysaccharide/SiO_2 ratio and from 0.085 to 0.099 g/g for the dye/SiO_2 ratio.

Functional Enzyme-Driven Controlled Release. As stated above the aim was to develop enzyme-triggered delivery systems using saccharide-capped mesoporous nanoscopic scaffolds. In this section, several experiments were carried out in order to study the enzyme-responsive controlled-release protocol, using the capped materials, in detail. The behavior of **S1**, **S2**, and **S3** in the presence of pancreatin and of solid **S4** in the presence of β-D-galactosidase was initially analyzed in water at pH 7.5, as these have been described as optimal conditions for enzyme-based degradation of saccharides. Pancreatin (a mixture of amylase, lipase, and proteases) would uncap the pores through selective hydrolysis of the 1 → 4 glycosidic bond in the starch chains, whereas β-D-galactosidase, able to hydrolyze 1 → 4 glycosidic bond between β-D-galactose and β-D-glucose, would induce the pores to open in **S4**.

In a typical experiment, **S1**, **S2**, **S3**, and **S4** were suspended in water at pH 7.5 in the presence of and in the absence of the corresponding enzyme. The suspension was then stirred and the dye delivery was monitored through the absorption band of the $[Ru(bipy)_3]^{2+}$ dye at 453 nm (Figure 4 shows the delivery profiles). As a significant feature, the "zero release" obtained in the absence of enzyme should be noted. This is especially relevant when analyzing solid **S3** (*vide infra*). In clear

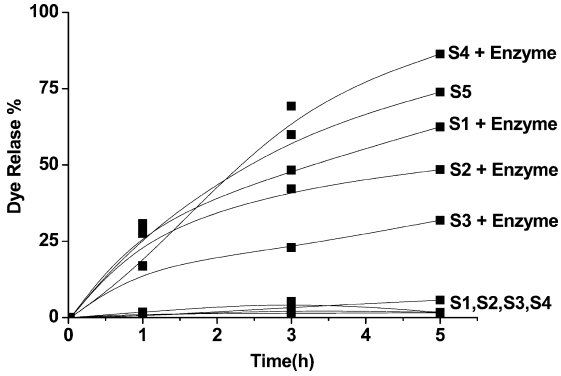

Figure 4. Kinetic release of $Ru(bipy)_3^{2+}$ dye from water suspensions of gated solids S1, S2, S3, S4 in the absence and in the presence of enzyme at pH 7.5, and water suspensions at pH 7.5 of solid S5, for 5 h.

contrast, the solids displayed an enzyme-dependent cargo delivery. In more detail, solids **S1**, **S2**, and **S3** released less than 2% of the entrapped dye after 5 h in water, whereas solid **S4** released 7% of its cargo. In the presence of the corresponding enzyme (pancreatin for **S1**, **S2**, and **S3** and β-D-galactosidase for **S4**) **S1**, **S2**, and **S3** delivered 63, 48, and 31% of the cargo, respectively, whereas solid **S4** released 85% of the dye (see Figure 4). It is clear that a simple choice of the hydrolysis degree of the starch has a dramatic influence in the delivery profile. Thus, at a certain time, **S1** is able to deliver more cargo than **S2**, and **S2** is able to deliver more cargo than **S3**, which is directly related to the different DE values of the hydrolyzed starch acting as capping scaffoldings; that is, the lesser the hydrolysis is, the lower is the delivery rate. Although the rate of hydrolysis using pancreatin (acting on **S1**, **S2**, and **S3**) and β-D-galactosidase (for **S4**) may not be the same, it is apparent from Figure 4 that in the presence of the corresponding enzyme the use of a disaccharide such as lactose as a capping system results in a higher delivery rate when compared with the use of hydrolyzed starch.

Another important feature of the prepared capped materials is the ability to release their cargo in a progressive fashion for prolonged periods of time. This is especially the case for **S1**, **S2**, and **S3**. These systems are able to deliver the cargo over a period of at least 60 h (not shown), a property that could be of special interest to avoid unwanted drug delivery peaks. Low delivery rates have been observed particularly for **S3** nanoparticles that release *ca.* 68% of the cargo after 60 h and would be active for longer periods of time. This progressive release could be related to a lowered degree of hydrolysis of the appended starch in **S3** when compared to **S1** or **S2**.

To confirm the proposed enzyme-mediated gating mechanism, solid **S5** was prepared, which is similar to **S1**−**S4** but contains the commercially available monosaccharide derivative *N*-(3-triethoxysilylpropyl)gluconamide on the surface. This is a suitable model bearing in mind that the enzymatic hydrolysis of the chain capping structures in **S1**−**S4** will ideally result in a unique glucose unit appended on the external surface of the solid. As can be observed in Figure 4, the saccharide-functionalized **S1**−**S4** showed a very low cargo release in the absence of the corresponding enzyme, whereas the monosaccharide-containing **S5** displays a significant $[Ru(bipy)_3]^{2+}$ delivery under similar experimental conditions. These results stress the conclusion that the delivery induced in the presence of pancreatin or β-D-galactosidase is due to the enzymatic-mediated rupture of the glycosidic bond and reduction in length of the saccharide chain at the surface. To further demonstrate that both pancreatin and β-D-galactosidase are responsible of the release of $[Ru(bipy)_3]^{2+}$ dye, additional experiments were carried

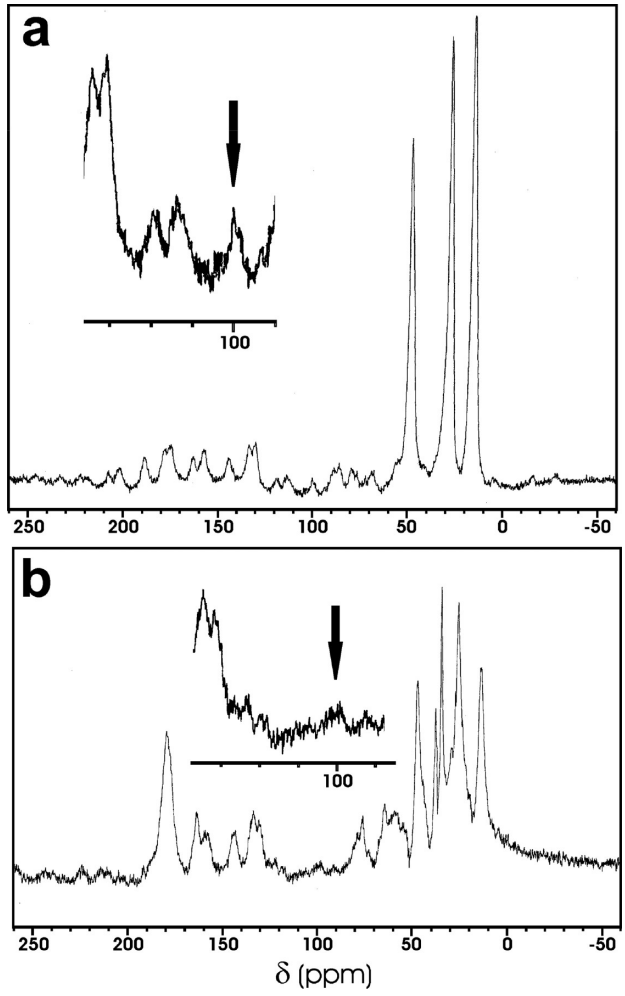

Figure 5. ^{13}C MAS NMR spectrum of (a) S1 and (b) S1-1.

out. First, the enzymes were denaturated by heating the solutions containing the enzymes (pH 7.5) at 60 °C for 60 min before the addition of **S1**−**S4**. In a second experiment, solids **S1**, **S2**, **S3**, and **S4** were incubated in the presence of the digestive protease pepsin. In both experimental settings no dye release was observed, strongly suggesting the selective activity of pancreatin or β-D-galactosidase enzymatic hydrolysis as the mechanism responsible of the opening of the mesopores.

To corroborate that the gating mechanism arises from the grafting of polysaccharides in the pore outlets of the MCM-41 scaffold, the hybrid material **S0** that contains only the $[Ru(bipy)_3]^{2+}$ dye in the pores and lacks the hydrolyzed starch derivatives **1**, **2**, **3** or the disaccharide derivative **4** was prepared. Aqueous suspensions at pH 7.5 of solid **S0** alone showed a very fast dye release; however, dye delivery was strongly inhibited when **S0** was in the presence of β-D-galactosidase or pancreatin, most likely due to an unselective adsorption of the enzyme on the external mesoporous surface through interactions with the silanol groups. This indicated that the grafting of the polysaccharides on the surface of mesoporous materials does not only act as capping systems that can be selectively uncapped but at the same time the functionalized surface with the saccharides prevent the unspecific adsorption of the enzymes.

To complete the study of the effect that the enzyme activity has on the saccharide, the solid **S1**-**1** (obtained from solid **S1** after the uncapping process using pancreatin and delivery of the entrapped dye) was prepared and ^{13}C NMR studies were carried out. The ^{13}C MAS NMR spectrum of samples **S1** and **S1-1** are shown in Figure 5. The ^{13}C NMR spectrum of **S1** displays signals in the 11−50 ppm range assigned to the 3-aminopropyltriethoxysilane linker, resonances between 70−90 ppm corresponding to the HO−C− units of the saccharide, and signals between 115−260 ppm attributed to the $[Ru(bipy)_3]^{2+}$ dye. Additionally, the characteristic ^{13}C signal of the (−O−CH−O−) glycosidic bond is clearly found in the **S1** solid at 100 ppm (see Figure 5). The ^{13}C NMR spectrum of solid **S1**-**1** still shows some signals at the above-mentioned shift ranges indicating the presence of certain saccharide still anchored to the solid and the presence of some undelivered dye that may remain stoutly adsorbed on the walls of the mesopores. However, the most remarkable feature in **S1-1** is the pronounced relative decrease of the ^{13}C signal intensity at 100 ppm, strongly indicating that the enzymatic hydrolysis of the glycosidic bonds was highly effective. In fact, a certain (low) proportion of nonhydrolyzed saccharides is reasonably expected in the **S1-1** due to some steric hindrance for the complete enzymatic attack. This could be the origin of the complex NMR spectra in the 11−50 ppm chemical shift range associated with mixtures of slightly different aminopropyl arms.

Delivery of Gated Materials in Intracellular Media. Cell internalization of mesoporous silica nanoparticles bearing gated stimuli-responsive scaffoldings is an appealing new interdisciplinary research field on the frontier of nanoscience.[79−89] As stated above one goal in this study was to demonstrate that easy-to-prepare saccharide-capped silica mesoporous nanoparticles could be used for in cell delivery applications. Thus, after the *in vitro* characterization of the different saccharide-capped mesoporous scaffolds (*vide ante*), **S1** nanoparticles were selected for further *ex vivo* assays. Previous reports suggested that saccharides can be used as targeting molecules in modified nanoparticles in order to induce efficient uptake by target cells *via* endocytosis.[90,91] Therefore, saccharide-capped SMPS could be good candidates for the design of intracellular cargo-releasing specialized nanodevices.

Initially, an evaluation of the ability of cells to internalize **S1** and the suitability of the nanoparticles in terms of cellular toxicity was performed (Figure 6). Confocal microscopy analysis was used in order to evaluate whether or not **S1** was internalized in both the tumoral HeLa and nontumoral LLC-PK1 cell lines (see Materials and Methods section for further information)

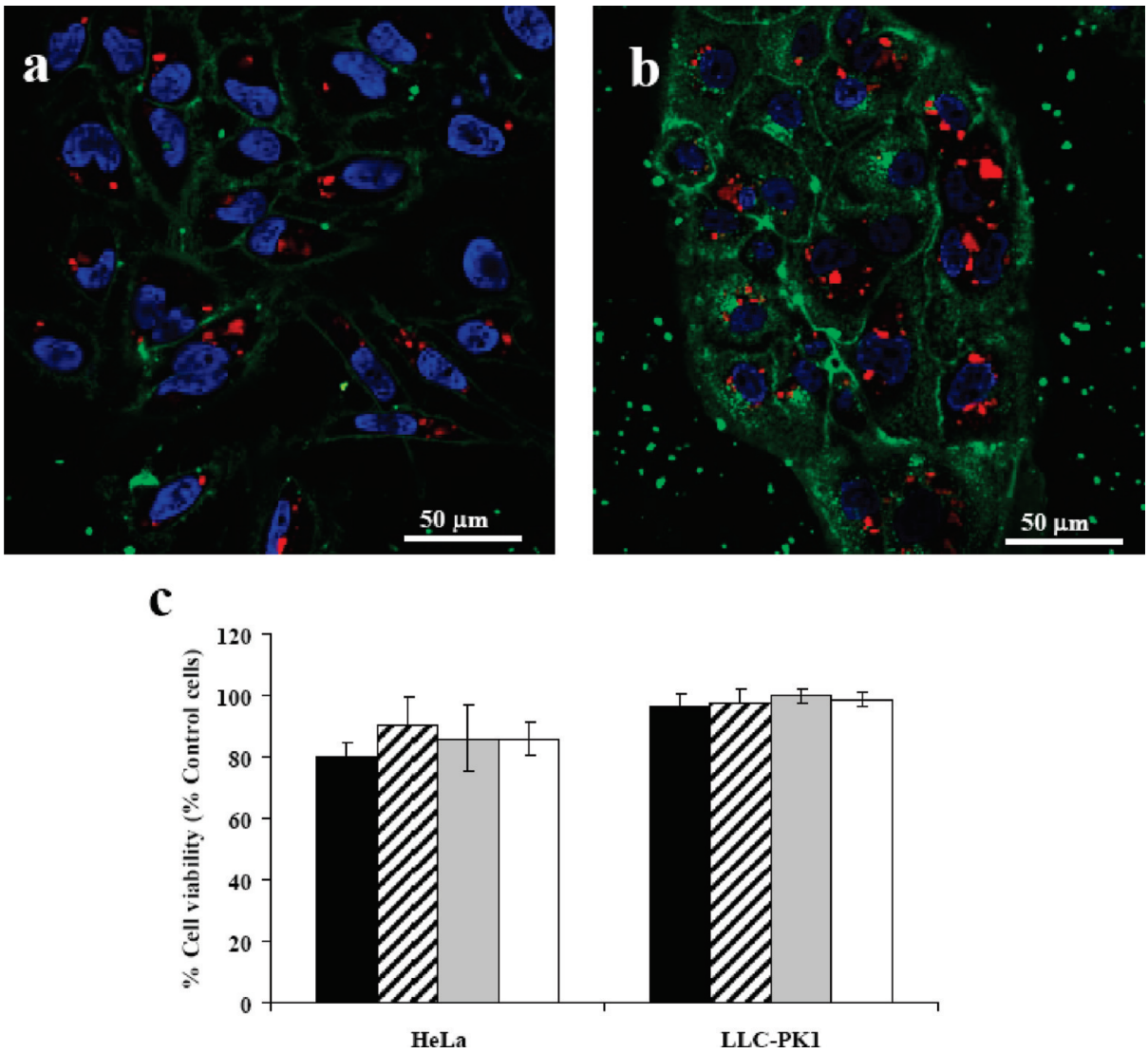

Figure 6. Cellular uptake of S1. (a) HeLa and (b) LLC-PK1 cells were incubated for 20 min in the presence of **S1** 50 μg/mL. Next, the medium was removed and fresh medium was added. After 15 h, confocal microcopy studies of **S1** cellular uptake were performed by means of $[Ru(bipy)_3]^{+2}$-**S1** associated fluorescence (red) in the presence of DNA marker Hoechst 33342 (blue) and the plasma membrane marker WGA Alexa Fluor 647 (green). For cell viability studies, (c) HeLa and LLC-PK1 cells were treated with **S1** in the same conditions at concentrations of 50, 25, 10, and 5 μg/mL (black, gray, striped, and white bars, respectively) for 24 h. Then, cell viability was quantified by means of a WST-1 assay. Three independent experiments were performed and data are reported as (mean ± s).

tracking the $[Ru(bipy)_3]^{+2}$ fluorescence. In these experiments cell nuclei were stained with Hoechst 33342 and cellular membrane with the fluorescent marker WGA Alexa Fluor 647 as cellular markers. A dotted pattern of a $[Ru(bipy)_3]^{+2}$ fluorescent signal associated to intracellular vesicles was observed (Figure 6 panels a and b for HeLa and LLC-PK1 cells, respectively) suggesting **S1** internalization in both cell lines. A WST-1 cell viability assay was employed to determine any unspecific toxicity of **S1**. The output of the assay suggested that **S1** was well tolerated by the cells in the experimental conditions (Figure 6c).

The presence of **S1**-containing intracellular vesicles suggested an endosomal (or endosomic)-mediated cellular internalization. Such a mechanism is generally used in cellular systems to transport different substrates to the autolysosomes for bulk degradation in an energy-dependent process.[92−94] Therefore it is conceivable to postulate that cargo-containing **S1** is transported to the autolysosomes where the activity of lysosome enzymes (including amylases) induces a saccharide hydrolysis-dependent release of the entrapped guest. To characterize the way **S1** nanoparticles are internalized, HeLa and LLC-PK1 cells were incubated in the presence of **S1** at 37 and 4 °C and the $[Ru(bipy)_3]^{+2}$ associated fluorescence was measured (Figure 7a,b). A statistically significant reduction of **S1** cellular uptake in both cell lines was observed upon incubating cells at 4 °C when compared to the uptake obtained at 37 °C. This fact would indicate an energy dependent internalization mechanism. Additionally, and interestingly, an increased uptake at all temperatures analyzed for tumoral HeLa cells when compared to nontumoral LLC-PK1 cells was observed. To

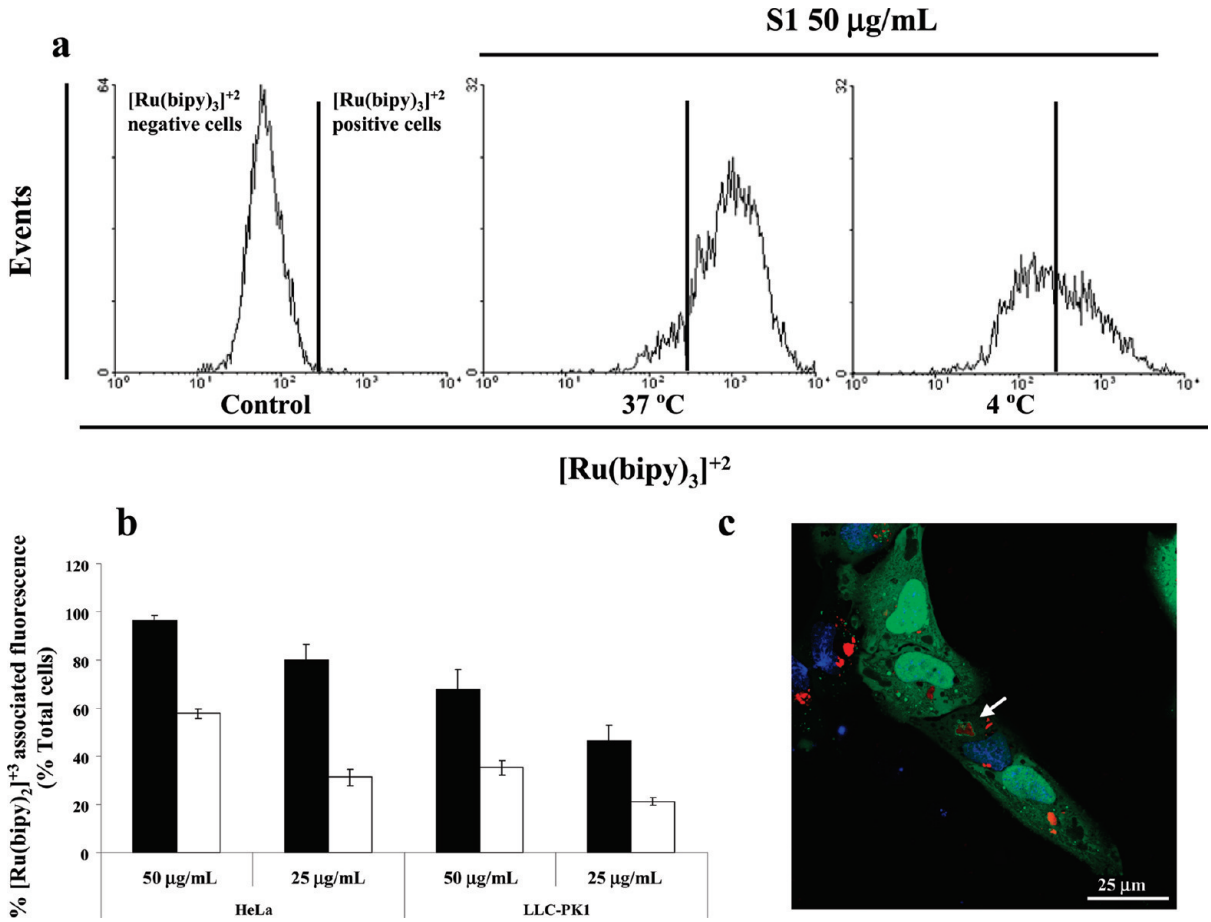

Figure 7. Implication of endosomes and lysosomes in the cellular degradation of S1. HeLa and LLC-PK1 cells were treated **S1** 50 and 25 μg/mL at 37 and 4 °C. After 20 min, nanoparticles were removed and cells were further incubated at 37 °C for 24 h. Then, $[Ru(bipy)_3]^{+2}$ associated fluorescence was studied by means of flow cytometry. In panel b, columns indicate the percentage of cells which stained positive for $[Ru(bipy)_3]^{+2}$ in HeLa and LLC-PK1 cells at 37 °C (black bars) and 4 °C (white bars), respectively. Three independent experiments were performed employing duplicates. Results are expressed as (mean ± s). Statistically significant data (Student's *t* test, $P < 0.05$) were obtained in all cases when comparing the two different incubation temperatures. To determine the autolysosomal localization of **S1** nanoparticles, HeLa cells were transfected with LC3-eGFP and 24 h later treated with **S1** 50 and 25 μg/mL for 20 min. After the treatment, the medium was changed and the cells were further incubated for 24 h prior to determination through confocal microscopy of the localization of $[Ru(bipy)_3]^{+2}$ associated fluorescence (red) and LC3-eGFP (green). As a result, autolysosomal localization of **S1** was determined (white arrow).

further characterize the internalization process, HeLa cells were transfected with the autolysosome marker microtubule-associated protein 1 light chain 3 (LC3-I) fusionated to the green fluorescent protein (GFP, LC3-eGFP).[95] The LC3-I protein presents a cytoplasmic localization under normal conditions. In the presence of inductors of autolysosome formation, it is processed and recruited to the autolysosomes, where LC3 II is generated by site specific proteolysis and lipidation near to the C-terminus. This fact induces the appearance of a dotted pattern related to the membrane associated LC3-II new subcellular localization. Once transfected, cells were treated with **S1** and the fluorescence associated to the $[Ru(bipy)_3]^{+2}$ dye was determined. As a result, a certain number of cells showed a dotted $[Ru(bipy)_3]^{+2}$ pattern surrounded by LC3-eGFP-associated vesicles suggesting that the actual location of cell internalized **S1** is in the autolysosomes (Figure 7c).

To prove the lysosomal amylase-mediated degradation of the capping saccharides of **S1**, new capped mesoporous nanoparticles were synthesized and loaded with the chemotherapeutic agent doxorubicin (dox) as a guest molecule (**S1**-**DOX**).[96] **S1**-**DOX** shows a similar N_2 adsorption−desorption isotherm, XRD profile, and TEM images to that observed for **S1** (data not shown). The content of dox in solid **S1**-**DOX** was determined by elemental and thermogravimetric analysis and amounted to 0.278 g of dox/g SiO_2. Kinetic release of dox from water suspensions of the gated **S1**-**DOX** solid in the presence and absence of enzyme at pH 7.5 were carried out, and a similar delivery behavior to that found for **S1** was observed; that is, zero delivery in the absence of amylases and delivery in the presence of the enzymes. On the basis of these observations *in vitro*, further *ex vivo* assays were carried out. Dox is broadly employed in the treatment of cancer. However, the nonspecific cell internalization of this drug causes

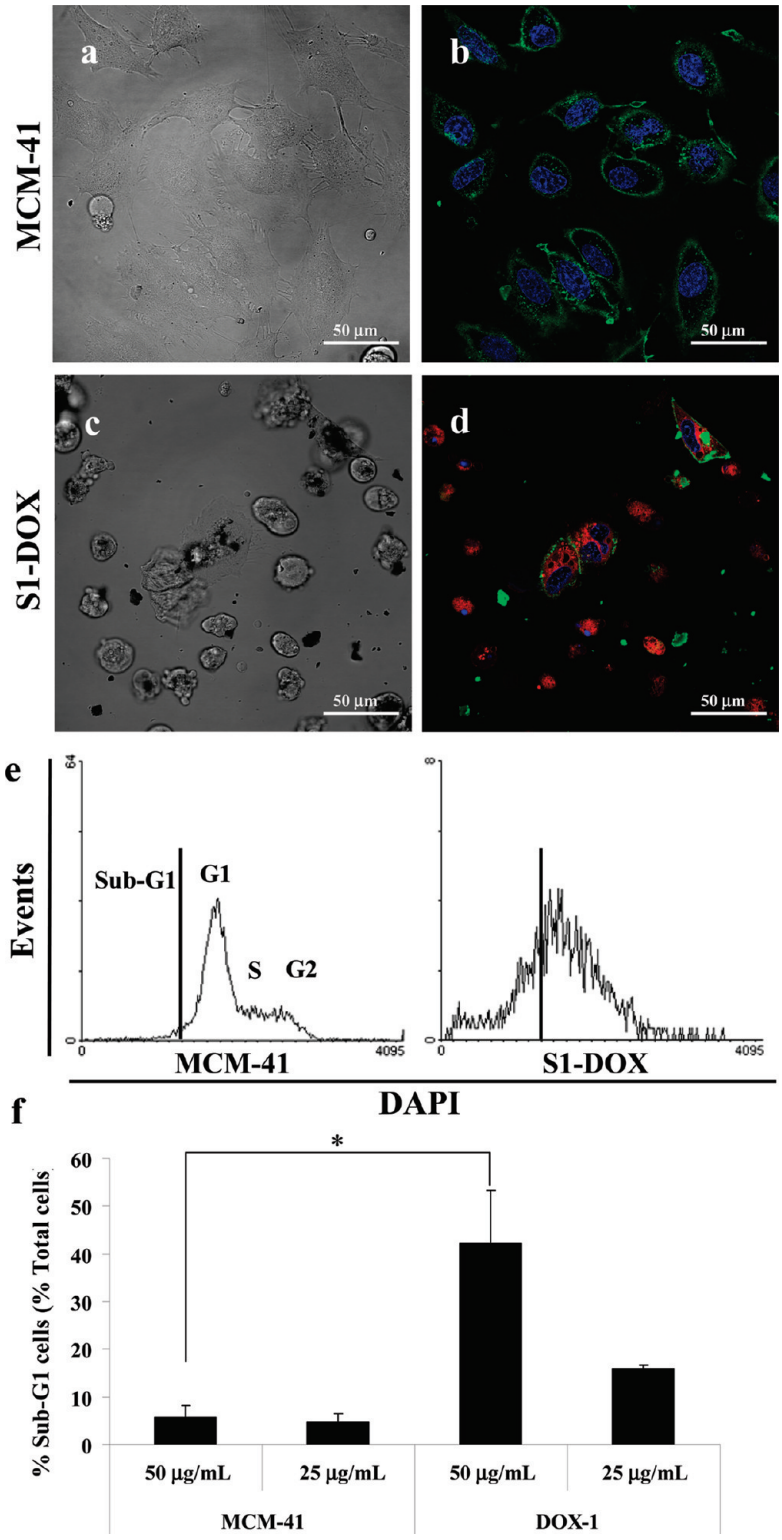

Figure 8. **S1-DOX** cell internalization induces cell death. HeLa cells were treated with control MCM-41 (a,b) or **S1-DOX** (c,d) at 50 and 25 µg/mL and after 20 min, the medium was removed, and cells were further incubated for 24 h. MCM-41-treated cells remained attached to the plate (a) and showed standard phenotype in confocal microscopy analysis (b) when nuclei were stained with Hoechst 33342 (blue) and plasma membrane with WGA Alexa Fluor 647 (green). In contrast, **S1-DOX**-treated cells were detached from the plate (c) and an in cell diffuse pattern of dox-associated fluorescence (red) together with cellular corpses were observed (d) suggesting dox-induced cell death. Quantification of cell death was performed by flow cytometry. DNA content was studied by fixing the cells in ethanol and staining them with DAPI. MCM-41 treated cells presented a standard cell cycle distribution, while a significant percentage of **S1-DOX** treated cells presented a sub-G1 DNA content proving the existence of cell death processes (Figure 8e). A quantification of the percentage of cells in sub-G1 phase is shown in Figure 8f. Two independent experiments were performed employing duplicates in both cases. Results are expressed as (mean ± s). An asterisk indicates statistically significant data (Student's *t* test, $P < 0.05$).

significant secondary effects in treated patients (that is, cardiotoxic and nephrotoxic effects). Confining dox in nanoparticles for more-specific cellular release has been reported to be an interesting strategy to decrease the unwanted secondary effects, thereby increasing the efficiency of this drug.[97] **S1**-**DOX** nanoparticles were added to the cells at different concentrations and cellular localization and cell toxicity was examined by confocal microscopy and flow cytometry after 24 h (Figure 8). As experimental controls, MCM-41 material and the supernatant of the **S1**-**DOX** suspension employed to treat the cells were also added in the same conditions as **S1**-**DOX**. MCM-41 was used in order to discard any toxic effect associated with the mesoporous material, while a **S1**-**DOX** suspension was employed to discard any unspecific aperture of the molecular gate outside the cells. A significant percentage of **S1**-**DOX**-treated cells detached from the plate, due to the activation of dox-induced cell death, were observed by confocal microscopy studies. By contrast, no cell death was observed in MCM-41-treated cells (Figure 8a−d) or in the case of the supernatant of the **S1**-**DOX** suspension (data not shown). These results strongly suggest that dox delivery is only observed upon **S1**-**DOX** internalization and enzyme-mediated aperture of the saccharide gate. The quantification of the percentage of cell death was performed by flow cytometry (measured by DNA content staining with DAPI). Cellular population in normal conditions typically distributes in a two-peak graphic depending on their DNA content, that is, cells in G1- or G2-phase, whereas a cell undergoing cell death usually presents a sub-G1 DNA content due to cellular fragmentation and subsequent DNA loss. A typical cell cycle distribution was observed in cells treated with MCM41 (Figure 8e). In the case of cells treated with **S1**-**DOX**, the typical cell cycle distribution was lost and a significant percentage of cells presented a sub-G1 DNA content corresponding to dead cells (Figure 8e−f). These results indicate that nanoscopic SMPS functionalized with saccharide derivatives are suitable supports for the delivery of entrapped molecules into cells for biological applications.

CONCLUSIONS

It has been demonstrated that the attachment of a hydrolyzed starch derivative as a gatekeeper on the surface of MSNs supports provides a suitable method for the design of mesoporous systems able to deliver the entrapped guest in the presence of suitable enzymes. Specifically, the mesoporous silica nanoparticles **S1**, **S2**, and **S3** containing different grafted starch derivatives (*i.e.*, Glucidex 47, Gludicex 39, and Glucidex 29) showing a different degree of hydrolysis were prepared. Additionally, for comparative purposes, solid **S4** containing a lactose derivative as a capping molecule was also prepared. Whereas the capped **S1**−**S4** solids showed "zero release", the same solids in water in the presence of pancreatin (for **S1**−**S3**) and galactosidase (for **S4**) released the cargo in a controlled fashion due to the enzyme-induced hydrolysis of the glycosidic bonds in the anchored saccharides. A clear control of the delivery rate was additionally found depending on the used hydrolyzed starch derivative. The delivery results indicate that it is possible to design different delivery profiles *via* a simple selection of the degree of hydrolyzation of the starch (*i.e.*, related to the lengths of different saccharide components and their relative proportions). It was shown that the saccharide-functionalized nanoparticles **S1** are efficiently taken up by both tumoral (HeLa) and nontumoral (LLC-PK1) cells, although a more efficient internalization in HeLa cells was observed. The cellular uptake of the nanoparticles occurs *via* endocytosis targeting them to the autolysosomes, where the capping polysaccharides are degraded by lysosomal enzymes and the cargo is delivered. Finally, the possible application of saccharide-functionalized nanoparticles as suitable delivery systems in cells of chemotherapeutic agents such as doxorubicin was demonstrated, and a substantial reduction of cell viability was observed in cells treated with solid **S1**-**DOX**. These results suggest that it might be possible to use bioscaffoldings (for instance saccharide as demonstrated here) as capping systems for the preparation of biocompatible delivery nanodevices based on silica mesoporous supports. The possibility of using these "bio-gates" which could be selectively opened by biomolecules (for instance enzymes) opens a wide range of possibilities in the design of advanced nanodevices for controlled delivery applications, and a number of new advances in this area are anticipated.

EXPERIMENTAL SECTION

Synthesis. General Methods. XRD, TGA, elemental analysis, TEM, N_2 adsorption−desorption, NMR, and UV−visible spectroscopy techniques were employed to characterize the synthesized materials. Powder X-ray measurements were performed on a Philips D8 Advance diffractometer using Cu Kα radiation. Thermogravimetric analyses were carried out on a TGA/SDTA 851e Mettler Toledo balance, using an oxidant atmosphere (air, 80 mL/min) with a heating program consisting of a heating ramp of 10 °C per minute from 393 to 1273 K and an isothermal heating step at this temperature for 30 min. TEM images were obtained with a 100 kV Philips CM10 microscope. N_2 adsorption−desorption isotherms were recorded with a Micromeritics ASAP2010 automated sorption analyzer. The samples were degassed at 120 °C in vacuum overnight. The specific surface areas were calculated from the adsorption data in the low pressure range using the BET model. Pore size was determined following the BJH method. ^{1}H and ^{13}C nuclear magnetic resonance (NMR) spectra were acquired with a Varian 300 spectrometer (Sunnyvale, CA, USA). ^{13}C MAS NMR spectrum was re-

corded on a Varian Unity 300 spectrometer operating at 128.3 MHz using a magic angle spinning speed of 4.0 kHz. UV−visible spectroscopy was carried out with a Lambda 35 UV/vis spectrometer (Perkin-Elmer Instruments). Live cellular internalization studies were performed with a Cytomics FC 500 (Beckman Coulter Inc.) and a confocal Leica microscope handled with a TCS SP2 system, equipped with an acoustic optical beam splitter (AOBS). Cell viability measurements were carried out with a Wallac 1420 workstation.

Chemicals. The chemicals tetraethylorthosilicate (TEOS), *n*-cetyltrimethylammonium bromide (CTABr), sodium hydroxide (NaOH), 3-aminopropyltriethoxysilane, tris (2,2′-bipyridyl) ruthenium(II) chloride hexahydrate([$Ru(bipy)_3$]$Cl_2 \cdot 6H_2O$), Pancreatin from porcine pancreas, β-D-galactosidase from *Kluyveromyces lactis*, D-(+)-lactose monohydrate, and tissue culture grade dimethylsulfoxide (DMSO) were provided by Aldrich. *N*-(3-Triethoxysilylpropyl) gluconamide was provided by ABCR. The hydrolyzed starch Glucidex 47 (5% glucose, 50% maltose, 45% oligosaccharides and polysaccharides), Glucidex 39 (3% glucose, 37% maltose, 60% oligosaccharides and polysaccharides) and Glucidex 29 (10% glucose, 9% maltose, 81% oligosaccharides and polysaccharides) were provided by Roquette. D-MEM with L-glutamine, fetal calf serum (FCS), trypan blue solution (0.4%) cell culture grade, trypsin, wheat germ agglutinin Alexa Fluor 647, and Hoechst 33342 were provided by Gibco-Invitrogen. The cell proliferation reagent WST-1 was obtained from Roche Applied Science. Doxorubicin hydrochloride was provided by Sequoia Research Products, Ltd. All the products were used as received.

Synthesis of the Hydrolyzed Starch Derivative 1, 2, 3 (Scheme 2). A solution of 3-aminopropyltriethoxysilane (5.85 mL, 25 mmol) in ethanol was added to a suspension of hydrolyzed starch (Glucidex 47, Glucidex 39, and Glucidex 29) in ethanol (total volume 250 mL). The reaction mixture was stirred for 24 h at room temperature and then heated at 60 °C for 30 min. The solvent was evaporated under reduced pressure to give a white solid: **1**, 7.32 g, yield 84%; **2**, 7.15 g, yield 82%; **3**, 7.55 g, yield 87%. ^{1}H NMR (300 MHz, D_2O): δ 0.42 (t, 2H, $-CH_2-Si-$), 1.02 (t, 9 H, $CH_3-CH_2-O-Si-$), 1.53 (m, 2H, $-CH_2-CH_2-Si-$), 2.74 (t, 2H, $-NH-CH_2-CH_2-CH_2-Si-$), 3.20−3.77 (m, n H, starch hydrolyzed, $CH_3-CH_2-O-Si-$), 5.13 (d, 1 H, $-O-CH-O-$) ppm. ^{13}C{1H} NMR (75 MHz, D_2O): δ 9.62 ($-CH_2-Si-$), 16.65 ($CH_3-CH_2-O-Si-$), 21.74 ($-CH_2-CH_2-Si-$), 41.96 ($-NH-CH_2-CH_2-CH_2-Si-$), 57.25 ($CH_3-CH_2-O-Si-$), 61.84 ($HO-CH_2-CH-$), 72.67−78.11 ($HO-CH-$), 89.57 ($-O-CH-CH$), 94.84 ($-O-CH-NH-$), 100.25 ($-O-CH-O-$) ppm.

Synthesis of the Lactose Derivative 4 (Scheme 2). A solution of 3-aminopropyltriethoxysilane (5.85 mL, 25 mmol) in ethanol was added to a suspension of lactose monohydrate (5.4 g, 15 mmol), in ethanol (total volume 250 mL). The reaction mixture was stirred for 24 h at room temperature and then heated at 60 °C for 30 min. The solvent was evaporated under reduced pressure to give a white solid: **4**, 7.22 g, 13.24 mmol, yield 89%. ^{1}H NMR (300 MHz, D_2O): δ 0.46 (t, 2H, $-CH_2-Si-$), 1.03 (t, 9 H, $CH_3-CH_2-O-Si-$), 1.56 (m, 2H, $-CH_2-CH_2-Si-$), 2.77 (t, 2H, -$NH-CH_2-CH_2-CH_2-Si-$), 3.34−3.93 (m, 19 H, Lactose, $CH_3-CH_2-O-Si-$), 4.29 (d, 1 H, $-O-CH-O-$) ppm. ^{13}C{1H} NMR (75 MHz, D_2O): δ 10.89 ($-CH_2-Si-$), 17.52 ($CH_3-CH_2-O-Si-$), 23.32 ($-CH_2-CH_2-Si-$), 43.18 ($-NH-CH_2-CH_2-CH_2-Si-$), 58.17 ($CH_3-CH_2-O-Si-$), 61.77 ($HO-CH_2-CH-$), 69.31 ($HO-CH-$),71.72 ($HO-CH-$), 73.27 ($HO-CH-$), 76.11 ($-O-CH-CH$), 79.19 ($-O-CH-NH-$), 103.68 ($-O-CH-O-$) ppm. Mass spectra (M = $C_{21}H_{43}NO_{13}Si$): 545 (M + 1), 461 (M − (CH_3-CH_2-)$_3$), 369 (M − (CH_3-CH_2-O-)$_3-Si-CH_2-$), 326 (M − (CH_3-CH_2-O-) 3-$Si-CH_2-CH_2-CH_2-NH-$), 221 (M − lactose), 135 (M − lactose−$NH-CH_2-CH_2-CH_2-Si-$).

Synthesis of Mesoporous MCM-41 Nanoparticles. The MCM-41 mesoporous nanoparticles were synthesized using the following procedure: *n*-cetyltrimethylammoniumbromide (CTABr, 2.00 g, 5.48 mmol) was first dissolved in 960 mL of deionized water. NaOH (aq) (2.00 M, 7.00 mL) was added to the CTABr solution, followed by adjusting the solution temperature to 95 °C. TEOS (10.00 mL, $5.14.10^{-2}$ mol) was then added dropwise to the surfactant solution. The mixture was allowed to stir for 3 h to give a white precipitate. The solid product was centrifuged and washed with deionized water and ethanol. Finally the solid was dried at 60 °C (MCM-41 as-synthesized). To prepare the final porous material (MCM-41), the as-synthesized solid was calcined at 550 °C using an oxidant atmosphere for 5 h in order to remove the template phase.

Synthesis of S1, S2, S3 (Scheme 1). In a typical synthesis, 1.00 g of templated-free MCM-41 and the dye tris(2,2′-bipyridyl) ruthenium(II) chloride (0.6 g, 0.8 mmol) were suspended in 40 mL of water in a round-bottomed flask under inert atmosphere. The mixture was stirred for 24 h at room temperature with the aim of achieving the maximum loading in the pores of the MCM-41 scaffolding. Then, an excess of the corresponding alkoxysilane derivative **1**, **2**, and **3** (1 g) in 20 mL of water was added and the final mixture was stirred for 5.5 h at room temperature. Finally, the solid (**S1**, **S2**, **S3**) was filtered off, washed with 40 mL of water, and dried at 40 °C for 12 h.

Synthesis of S1-DOX. In a typical synthesis, 1.00 g of templated-free MCM-41 and doxorubicin hydrochloride (0.5 g, 0.91 mmol) were suspended in 40 mL of water in a round-bottomed flask under inert atmosphere. The mixture was stirred for 24 h at room temperature with the aim of achieving the maximum loading in the pores of the MCM-41 scaffolding. Then, an excess of the alkoxysilane derivative **1** (1 g) in 20 mL of water was added, and the final mixture was stirred for 5.5 h at room temperature. Finally, the solid (**S1**-**DOX**) was filtered off, washed with 40 mL of water, and dried at 40 °C for 12 h.

Synthesis of S4. (Scheme 1). In a typical synthesis, 1.00 g of templated-free MCM-41 and the dye tris(2,2′-bipyridyl) ruthenium(II) chloride (0.6 g, 0.8 mmol) were suspended in 40 mL of water in a round-bottomed flask under inert atmosphere. The mixture was stirred for 24 h at room temperature with the aim of achieving the maximum loading in the pores of the MCM-41 scaffolding. Then, an excess of the alkoxysilane derivative **4** (1 g, 1.8 mmol) in 20 mL of water was added, and the final mixture was stirred for 5.5 h at room temperature. Finally, the solid (**S4**) was filtered off, washed with 40 mL of water, and dried at 40 °C for 12 h.

Synthesis of S5. (Scheme 1). A 1.0 g portion of templated-free MCM-41 and the dye tris(2,2′-bipyridyl)ruthenium(II) chloride (0.6 g, 0.8 mmol) were suspended in 40 mL of anhydrous acetonitrile and heated at 120 °C in a Dean−Stark in order to remove the adsorbed water by azeotropic distillation under inert atmosphere. The suspension was stirred for 24 h at room temperature with the aim of loading the pores of the MCM-41 scaffolding. After this, an excess of the commercially available *N*-(3-triethoxysilylpropyl)gluconamide (50% in ethanol, 1.05 mL, 1.31 mmol) was added and the suspension was stirred for 5.5 h. The final orange solid (**S5**) was filtered, washed with acetonitrile, and dried at 40 °C for 12 h.

Synthesis of S6. In a typical synthesis, 1.00 g of templated-free MCM-41 was suspended in 40 mL of water in a round-bottomed flask under inert atmosphere, an excess of the alkoxysilane derivative **1** (1 g) was added, and the mixture was stirred for 5.5 h at room temperature. Finally, the solid **S6** was filtered off, washed with 40 mL of water, and dried at 40 °C for 12 h.

Synthesis of S0. For the sake of comparison, and as a control solid, hybrid material containing only the $[Ru(bipy)_3]^{2+}$ dye (**S0**) was synthesized in order to assess the effect of the saccharide grafted in the outer of the MCM-41 pores. The procedure was the same as described for **S1**, **S2**, **S3**, and **S4** but without grafting the saccharide derivative. The final orange solid (**S0**) was filtered, washed with water, and dried at 40 °C for 12 h.

Dye Release Studies. In a typical experiment, 10 mg of **S1**, **S2**, **S3**, and **S4** were suspended in 18.75 mL of water at pH 7.5 and then 6.25 mL of enzyme solution (0.4 g of enzyme in 100 mL of water at pH 7.5) was added. Pancreatin was used for solids **S1**, **S2**, **S3** and β-D-galactosidase for solid **S4**. The suspensions were used for the evaluation of the gate-like effect by studying dye release from the pore voids of the functionalized material *via* the rupture of a glycosidic bond. For release studies with **S0** and **S5** 10 mg of the solid were placed in 25 mL of water at pH 7.5 and at a certain time an aliquot was separated and filtered. The delivery of the dye from the pore voids to the aqueous solution was monitorized *via* the absorbance of the dye at 453 nm.

Cell Culture Conditions. The HeLa human cervix adenocarcinoma and the LLC-PK1 pig kidney cells were purchased from the German Resource Centre for Biological Materials (DSMZ) and were grown in D-MEM and Medium 199 supplemented with 10% and 6% FCS, respectively. Cells were maintained at 37 °C in an atmosphere of 5% carbon dioxide and 95% air and underwent passage twice a week. Cells were transfected with eGFP-C1 plasmid containing the rat LC3 gene (LC3-eGFP) (kindly provided by G. Kroemer) by means of lipofectamine transfection reagent (Invitrogen), according to the manufacturer's recommendations.

WST-1 Cell Viability Assay. Cells were cultured in sterile 96-well microtiter plates at a seeding density of 2.5×10^3 and 8×10^3 cells/well for HeLa and LLC-PK1, respectively, and they were allowed to settle for 24 h. **S1** in DMSO was added to cells at a final concentration of 50, 25, 10, and 5 μg/mL. After 23 h, WST-1[98] (10 μL of a 5 mg/mL solution) was added to each well. Cells were further incubated for 1 h (a total of 24 h of incubation was therefore studied), and absorbance was measured at 595 nm.

Live Confocal Microscopy S1 Cellular Internalization. HeLa and LLC-PK1 cells were seeded in 24 mm Φ glass coverslips in six-well plates at a seeding density of 10^5 cells/well. After 24 h, cells were treated when indicated with **S1** or **S1**-**DOX** at a final concentration of 50 μg/mL. After 20 min, the medium was removed to eliminate compounds. After 15 h of incubation, cells were stained with 10 ng/mL of Hoechst 33342 and 5 mg/mL wheat germ agglutinin (WGA) Alexa Fluor 647 for 30 min in PBS containing 10% FCS or keeping the medium in case of **S1**-**DOX** treatments. Slides were visualized under a confocal microscope.

Cytofluorometry Studies Employing S1. To develop the cytofluorometry studies, HeLa and LLC-PK1 cells were seeded at 50×10^3 cells/well in a 12-well plate. After 24 h, cells were treated with **S1**-**DOX** 50 μg/mL for 20 min before removing the culture medium. Cells were incubated for 15 h before fixing them with ethanol 80%, keeping them at −20 °C for 24 h. Finally, cells were stained with DAPI Concentration, and cell cycle studies were performed to determine the cell viability of the samples.

Acknowledgment. The authors wish to express their gratitude to the Spanish Government (Projects MAT2009-14564-C04-01, MAT2009-14564-C04-04 and BIO2007-60066) and the Generalitat Valencia (Projects PROMETEO/2009/016 and PROMETEO/2010/005) for support. A.B. is grateful to the Universidad Politécnica de Valencia for an FPI grant. E.A. thanks the MICINN for a FPU contract. We thank Roquette for the Glucidex samples. We would like to thank the CIPF confocal microscopy service for technical support.

REFERENCES AND NOTES

1. Hoste, K.; De Winne, K.; Schacht, E. Polymeric Prodrugs. *Int. J. Pharm.* **2004**, *277*, 119–131.
2. Liu, S.; Maheshwari, R.; Kiick, K. L. Polymer-Based Therapeutics. *Macromolecules* **2009**, *42*, 3–13.
3. Traitel, T.; Goldbart, R.; Kost, J. Smart Polymers for Responsive Drug-Delivery Systems. *J. Biomater. Sci., Polym. Ed.* **2008**, *19*, 755–767.
4. Puoci, F.; Iemma, F.; Picci, N. Stimuli-Responsive Molecularly Imprinted Polymers for Drug Delivery: A Review. *Curr. Drug Delivery* **2008**, *5*, 85–96.
5. Siepmann, F.; Siepmann, J.; Walther, M.; MacRae, R.; Bodmeier, R. Polymer Blends for Controlled Release Coatings. *J. Controlled Release* **2008**, *125*, 1–15.
6. Harrison, K. Introduction to Polymeric Drug Delivery Systems. *Biomedical Polymers*; Woodhead: Cambridge, UK, 2007; pp 33−56.
7. Nair, L. S.; Laurenciana, C. T. Biodegradable Polymers As Biomaterials. *Prog. Polym. Sci.* **2007**, *32*, 762–798.
8. Schmaljohann, D. Thermo- and pH-Responsive Polymers in Drug Delivery. *Adv. Drug Delivery Rev.* **2006**, *58*, 1655–1670.
9. Vallet-Regí, M.; Balas, F.; Arcos, D. Mesoporous Materials for Drug Delivery. *Angew.Chem., Int. Ed.* **2007**, *46*, 7548–7558.
10. Vallet-Regí, M.; Rámila, A.; del Real, R. P.; Pérez-Pariente, J. A New Property of MCM-41: Drug Delivery System. *J. Chem. Mater.* **2001**, *13*, 308–311.
11. Muñoz, B.; Rámila, A.; Pérez-Pariente, J.; Díaz, M.; Vallet-Regí, I. MCM-41 Organic Modification as Drug Delivery Rate Regulator. *Chem. Mater.* **2003**, *15*, 500–503.
12. Hoffmann, F.; Cornelius, M.; Morell, M.; Fröba, M. Silica-Based Mesoporous Organic−Inorganic Hybrid Materials. *Angew. Chem., Int. Ed.* **2006**, *45*, 3216–3251.
13. Descalzo, A. B.; Martínez-Máñez, R.; Sancenón, F.; Hoffmann, K.; Rurack, K. The Supramolecular Chemistry of Organic−Inorganic Hybrid Materials. *Angew. Chem., Int. Ed.* **2006**, *45*, 5924–5948.
14. Saha, S.; Leung, K. C. F.; Nguyen., N. T.; Stoddart, J. F.; Zink, J. I. Nanovalves. *Adv. Funct. Mater.* **2007**, *17*, 685–693.
15. Trewyn, B. G.; Slowing, I. I.; Giri, S; Chen, H. T.; Lin, V.S.-Y. Synthesis and Functionalization of a Mesoporous Silica Nanoparticle Based on the Sol-Gel Process and Applications in Controlled Release. *Acc. Chem. Res.* **2007**, *40*, 846–853.
16. Slowing, I. I.; Vivero-Escoto, J. L.; Wu, C. W.; Lin, V.S.-Y. Mesoporous Silica Nanoparticles as Controlled Release Drug Delivery and Gene Transfection Carriers. *Adv. Drug Delivery Rev.* **2008**, *60*, 1278–1288.
17. Aznar, E.; Martínez-Máñez, R.; Sancenón, F. Controlled Release Using Mesoporous Materials Containing Gate-like Scaffoldings. *Expert Opin. Drug Delivery* **2009**, *6*, 643–655.
18. Cotí, K. K.; Belowich, M. E.; Liong, M.; Ambrogio, M. W.; Lau, Y. A.; Khatib, H. A.; Zink, J. I.; Khashab, N. M.; Stoddart, J. F. Mechanised Nanoparticles for Drug Delivery. *Nanoscale* **2009**, *1*, 16–39.
19. Johansson, E.; Choi, E.; Angelos, S.; Liong, M.; Zink, J. I. Light-Activated Functional Mesostructured Silica. *Sol-Gel Sci. Technol.* **2008**, *46*, 313–322.
20. Leung, K. C.-F.; Chak, C.-P.; Lo, C.-M.; Wong, W.-Y.; Xuan, S.; Cheng, C. H. K. pH-Controllable Supramolecular Systems. *Chem. Asian J.* **2009**, *4*, 364–381.
21. Mal, N. K.; Fujiwara, M.; Tanaka, Y. Photocontrolled Reversible Release of Guest Molecules from Coumarin-Modified Mesoporous Silica. *Nature* **2003**, *421*, 350–353.
22. Mal, N. K.; Fujiwara, M.; Tanaka, Y.; Taguchi, T.; Matsukata, M. Photoswitched Storage and Release of Guest Molecules in the Pore Void of Coumarin-Modified MCM-41. *Chem. Mater.* **2003**, *15*, 3385–3394.
23. Zhu, Y.; Fujiwara, M. Installing Dynamic Molecular Photomechanics in Mesopores: A Multifunctional Controlled-Release Nanosystem. *Angew. Chem., Int. Ed.* **2007**, *46*, 2241–2244.
24. Lu, J.; Choi, E.; Tamanoi, F.; Zink, J. I. Light-Activated Nanoimpeller-Controlled Drug Release in Cancer Cells. *Small* **2008**, *4*, 421–426.
25. Angelos, S.; Vhoi, E.; Vögtle, F.; De Cola, L.; Zink, J. I. Photo-Driven Expulsion of Molecules from Mesostructured Silica Nanoparticles. *J. Phys. Chem. C* **2007**, *111*, 6589–6592.
26. Liu, N.; Dunphy, D.; Atanassov, P.; Bunge, S. D.; Chen, Z.; López, G. P.; Boyle, T. J.; Brinker, C. J. Photoregulation of Mass Transport through a Photoresponsive Azobenzene-Modified Nanoporous Membrane. *Nano Lett.* **2004**, *4*, 551–554.
27. Ferris, D. P.; Zhao, Y.-L.; Khashab, N. M.; Khatib, H. A.; Stoddart, J. F.; Zink, J. I. Light-Operated Mechanized Nanoparticles. *J. Am. Chem. Soc.* **2009**, *131*, 1686–1688.
28. Park, C.; Lee, K.; Kim, C. Photoresponsive Cyclodextrin-Covered Nanocontainers and Their Sol-Gel Transition Induced by Molecular Recognition. *Angew. Chem., Int. Ed.* **2009**, *48*, 1275–1278.
29. Aznar, E.; Casasús, R.; García-Acosta, B.; Marcos, M. D.; Martínez-Máñez, R.; Sancenón, F.; Soto, J.; Amorós, P. Photochemical and Chemical Two-Channel Control of Functional Nanogated Hybrid Architectures. *Adv. Mater.* **2007**, *19*, 2228–2231.
30. Casasús, R.; Marcos, M. D.; Martínez-Máñez, R.; Ros-Lis, J. V.; Soto, J.; Villaescusa, L. A.; Amorós, P.; Beltrán, D.; Guillem, C.; Latorre, J. Toward the Development of Ionically Controlled Nanoscopic Molecular Gates. *J. Am. Chem. Soc.* **2004**, *126*, 8612–8613.
31. Casasús, R.; Climent, E.; Marcos, M. D.; Martínez-Máñez, R.;

Sancenón, F.; Soto, J.; Amorós, P.; Cano, J.; Ruiz, E. Dual Aperture Control on pH- and Anion-Driven Supramolecular Nanoscopic Hybrid Gate-like Ensembles. *J. Am. Chem. Soc.* **2008**, *130*, 1903–1917.
32. Bernardos, A.; Aznar, E.; Coll, C.; Martínez-Máñez, R.; Barat, J. M.; Marcos, M. D.; Sancenón, F.; Soto, J. Controlled Release of Vitamin B_2 Using Mesoporous Materials Fucntionalized with Amine-Bearing Gate-like Scaffoldings. *J. Controlled Release* **2008**, *131*, 181–189.
33. Yang, Q.; Wang, S.; Fan, P.; Wang, L.; Di, Y.; Lin, K.; Xiao, F.-S. pH-Responsive Carrier System Based on Carboxylic Acid Modified Mesoporous Silica and Polyelectrolyte for Drug Delivery. *Chem. Mater.* **2005**, *17*, 5999–6003.
34. Nguyen, T. D.; Leung, K.C.-F.; Liong, M.; Pentecost, C. D.; Stoddart, J. F.; Zink, J. I. Construction of a pH-Driven Supramolecular Nanovalve. *Org. Lett.* **2006**, *8*, 3363–3366.
35. Leung, K.C.-F.; Nguyen, T. D.; Stoddart, J. F.; Zink, J. I. Supramolecular Nanovalves Controlled by Proton Abstraction and Competitive Binding. *Chem. Mater.* **2006**, *18*, 5919–5928.
36. Park, C.; Oh, K.; Lee, S. C.; Kim, C. Controlled Release of Guest Molecules from Mesoporous Silica Particles Based on a pH-Responsive Polypseudorotaxane Motif. *Angew. Chem., Int. Ed.* **2007**, *46*, 1455–1457.
37. Angelos, S.; Yang, Y.-W.; Khashab, N. M.; Stoddart, J. F.; Zink, J. I. Dual-Controlled Nanoparticles Exhibiting AND Logic. *J. Am. Chem. Soc.* **2009**, *131*, 11344–11346.
38. Angelos, S.; Yang, Y.-W.; Patel, K.; Stoddart, J. F.; Zink, J. I. pH-Responsive Supramolecular Nanovalves Based on Cucurbit[6]uril Pseudorotaxanes. *Angew. Chem., Int. Ed.* **2008**, *47*, 2222–2226.
39. Khashab, N. M.; Belowich, M. E.; Trabolsi, A.; Friedman, D. C.; Valente, C.; Lau, Y.; Khatib, H. A.; Zink, J. I.; Stoddart, J. F. pH-Responsive Mechanised Nanoparticles Gated by Semirotaxanes. *Chem. Commun.* **2009**, *2009*, 5371–5373.
40. Angelos, S.; Khashab, N. M.; Yang, Y.-W.; Trabolsi, A.; Khatib, H. A.; Stoddart, J. F.; Zink, J. I. pH Clock-Operated Mechanized Nanoparticles. *J. Am. Chem. Soc.* **2009**, *131*, 12912–12914.
41. Khashab, N. M.; Trabolsi, A.; Lau, Y. A.; Ambrogio, M. W.; Friedman, D. C.; Khatib, H. A.; Zink, J. I.; Stoddart, J. F. Redox- and pH-Controlled Mechanized Nanoparticles. *Eur. J. Org. Chem.* **2009**, *2009*, 1669–1673.
42. Du, L.; Liao, S.; Khatib, H. A.; Stoddart, J. F.; Zink, J. I. Controlled-Access Hollow Mechanized Silica Nanocontainers. *J. Am. Chem. Soc.* **2009**, *131*, 15136–15142.
43. Aznar, E.; Marcos, M. D.; Martínez-Máñez, R.; Sancenón, F.; Soto, J.; Amorós, P.; Guillem, C. pH- and Photo-Switched Release of Guest Molecules from Mesoporous Silica Supports. *J. Am. Chem. Soc.* **2009**, *131*, 6833–6843.
44. Trewyn, B. G.; Giri, S.; Slowing, I. I.; Lin, V.S.-Y. Mesoporous Silica Nanoparticle Based Controlled Release, Drug Delivery, and Biosensor Systems. *Chem. Commun.* **2007**, 3236–3245.
45. Trewyn, B. G.; Slowing, I. I.; Giri, S.; Chen, H.-T.; Lin, V.S.-Y. Synthesis and Functionalization of a Mesoporous Silica Nanoparticle Based on the Sol-Gel Process and Applications in Controlled Release. *Acc. Chem. Res.* **2007**, *40*, 846–853.
46. Lai, C.-Y.; Trewyn, B. G.; Jeftinija, D. M.; Jeftinija, K.; Xu, S.; Jeftinija, S.; Lin, V.S.-Y. A Mesoporous Silica Nanosphere-Based Carrier System with Chemically Removable CdS Nanoparticle Caps for Stimuli-Responsive Controlled Release of Neurotransmitters and Drug Molecules. *J. Am. Chem. Soc.* **2003**, *125*, 4451–4459.
47. Torney, F.; Trewyn, B. G.; Lin, V.S.-Y.; Wang, K. Mesoporous silica nanoparticles deliver DNA and chemicals into plants. *Nat. Nanotechnol.* **2007**, *2*, 295–300.
48. Radu, D. R.; Lai, C.-Y.; Jeftinija, K.; Rowe, E. W.; Jeftinija, S.; Lin, V.S.-Y. A Polyamidoamine Dendrimer-Capped Mesoporous Silica Nanosphere-Based Gene Transfection Reagent. *J. Am. Chem. Soc.* **2004**, *126*, 13216–13217.
49. Giri, S.; Trewyn, B. G.; Stellmaker, M. P.; Lin, V.S.-Y. Magnetic Nanoparticle-Capped Mesoporous Silica Nanorod-Based Stimuli-Responsive Controlled Release Delivery System. *Angew. Chem., Int. Ed.* **2005**, *44*, 5038–5044.
50. Slowing, I. I.; Trewyn, B. G.; Lin, V. S. -Y. Mesoporous Silica Nanoparticles for Intracellular Delivery of Membrane-Impermeable Proteins. *J. Am. Chem. Soc.* **2007**, *129*, 8845–8849.
51. Slowing, I. I.; Trewyn, B. G.; Giri, S.; Lin, V.S.-Y. Mesoporous Silica Nanoparticles for Drug Delivery and Biosensing Applications. *Adv. Funct. Mater.* **2007**, *17*, 1225–1236.
52. Vivero-Escoto, J. L.; Slowing, I. I.; Wu, C.-Y.; Lin, V.S.-Y. Photoinduced Intracellular Controlled Release Drug Delivery in Human Cells by Gold-Capped Mesoporous Silica Nanosphere. *J. Am. Chem. Soc.* **2009**, *131*, 3462–3463.
53. Mortera, R.; Vivero-Escoto, J.; Slowing, I. I.; Garrone, E.; Onida, B.; Lin, V.S.-Y. Cell-Induced Intracellular Controlled Release of Membrane Impermeable Cysteine from a Mesoporous Silica Nanoparticle-Based Drug Delivery System. *Chem. Commun.* **2009**, 321–3221.
54. Zhao, Y.; Trewyn, B. G.; Slowing, I. I.; Lin, V.S.-Y. Mesoporous Silica Nanoparticle-Based Double Drug Delivery System for Glucose-Responsive Controlled Release of Insulin and Cyclic AMP. *J. Am. Chem. Soc.* **2009**, *131*, 8398–8400.
55. Fujiwara, M.; Terashima, S.; Endo, Y.; Shiokawa, K.; Ohue, H. Switching Catalytic Reaction Conducted in Pore Void of Mesoporous Material by Redox Gate Control. *Chem. Commun.* **2006**, 4635–4637.
56. Liu, R.; Zhao, X.; Wu, T.; Feng, P. Tunable Redox-Responsive Hybrid Nanogated Ensembles. *J. Am. Chem. Soc.* **2008**, *130*, 14418–14419.
57. Liu, R.; Zhang, Y.; Feng, P. Multiresponsive Supramolecular Nanogated Ensembles. *J. Am. Chem. Soc.* **2009**, *131*, 15128–15129.
58. Hernandez, R.; Tseng, H.-R; Wong, J. W.; Stoddart, J. F.; Zink, J. I. An Operational Supramolecular Nanovalve. *J. Am. Chem. Soc.* **2004**, *126*, 3370–3371.
59. Nguyen, T. D.; Tseng, H.-R.; Celeste, P. C.; Flood, A. H.; Liu, Y.; Stoddart, J. F.; Zink, J. I. A Reversible Molecular Valve. *Proc. Natl. Acad. Sci., U.S.A.* **2005**, *102*, 10029–10034.
60. Nguyen, T. D.; Liu, Y.; Saha, S.; Leung, K.C.-F.; Stoddart, J. F.; Zink, J. I. Design and Optimization of Molecular Nanovalves Based on Redox-Switchable Bistable Rotaxanes. *J. Am. Chem. Soc.* **2007**, *129*, 626–634.
61. Nguyen, T. D.; Leung, K.C.-F.; Liong, M.; Liu, Y.; Stoddart, J. F.; Zink, J. I. Versatile Supramolecular Nanovalves Reconfigured for Light Activation. *Adv. Funct. Mater.* **2007**, *17*, 2101–2110.
62. Angelos, S.; Liong, M.; Choi, E.; Zink, J. I. Mesoporous Silicate Materials as Substrates for Molecular Machines and Drug Delivery. *Chem. Eng. J.* **2008**, *137*, 4–13.
63. Fu, Q.; Rao, G. V. R.; Ista, L. K.; Wu, Y.; Andrzejewski, B. P.; Sklar, L. A.; Ward, T. L.; López, G. P. Control of Molecular Transport Through Stimuli-Responsive Ordered Mesoporous Materials. *Adv. Mater.* **2003**, *15*, 1262–1266.
64. Coll, C.; Casasús, R.; Aznar, E.; Marcos, M. D.; Martínez-Máñez, R.; Sancenón, F.; Soto, J.; Amorós, P. Nanoscopic Hybrid Systems with a Polarity-Controlled Gate-like Scaffolding for the Colorimetric Signalling of Long-Chain Carboxylates. *Chem. Commun.* **2007**, 1957–1959.
65. Casasús, R.; Aznar, E.; Marcos, M. D.; Martínez-Máñez, R.; Sancenón, F.; Soto, J.; Amorós, P. New Methods for Anion Recognition and Signaling Using Nanoscopic Gatelike Scaffoldings. *Angew. Chem., Int. Ed.* **2006**, *45*, 6661–6664.
66. Aznar, E.; Coll, C.; Marcos, M. D.; Martínez-Máñez, R.; Sancenón, F.; Soto, J.; Amorós, P.; Cano, J.; Ruíz, E. Borate-Driven Gatelike Scaffolding Using Mesoporous Material Functionalised with Saccharides. *Chem.—Eur. J.* **2009**, *15*, 6877–6888.
67. Climent, E.; Marcos, M. D.; Martínez-Máñez, R.; Sancenón, F.; Soto, J.; Rurack, K.; Amorós, P. The Determination of Methylmercury in Real Samples Using Organically Capped Mesoporous Inorganic Materials Capable of Signal Amplification. *Angew. Chem., Int. Ed.* **2009**, *48*, 8519–8522.
68. Climent, E.; Bernardos, A.; Martínez-Máñez, R.; Maquieira, A.; Marcos, M. D.; Pastor-Navarro, N.; Puchades, R.;

Sancenón, F.; Soto, J.; Amorós, P. Controlled Delivery Systems Using Antibody-Capped Mesoporous Nanocontainers. *J. Am. Chem. Soc.* **2009**, *131*, 14075–14080.
69. Patel, K.; Angelos, S.; Dichtel, W. R.; Coskun, A.; Yang, Y.-W.; Zink, J. I.; Stoddart, J. F. Enzyme-Responsive Snap-Top Covered Silica Nanocontainers. *J. Am. Chem. Soc.* **2008**, *130*, 2382–2383.
70. Klichko, Y.; Khashab, N. -M.; Yang, Y. -W.; Angelos, S.; Stoddart, J. F.; Zink, J. I. Improving Pore Exposure in Mesoporous Silica Films for Mechanized Control of the Pores. *Microporous Mesoporous Mater.* **2010**, *132*, 435–441.
71. Schlossbauer, A.; Kecht, J.; Bein, T. Biotin-Avidin as a Protease-Responsive Cap System for Controlled Guest Release from Colloidal Mesoporous Silica. *Angew. Chem., Int. Ed.* **2009**, *48*, 3092–3095.
72. Bernardos, A.; Aznar, E.; Marcos, M. D.; Martínez-Máñez, R.; Sancenón, F.; Soto, J.; Barat, J. M.; Amorós, P. Enzyme-Responsive Controlled Release Using Mesoporous Silica Supports Capped with Lactose. *Angew. Chem., Int. Ed.* **2009**, *48*, 5884–5887.
73. Park, C.; Kim, H.; Kim, S.; Kim, C. Enzyme Responsive Nanocontainers with Cyclodextrin Gatekeepers and Synergistic Effects in Release of Guests. *J. Am. Chem. Soc.* **2009**, *131*, 16614–16615.
74. Starch is a polysaccharide carbohydrate consisting of a large number of glucose units linked together by glycosidic bonds. Starch is a product of plant metabolism that consists of two types of molecules; *i.e.,* the linear amylose (20−25%) and the branched amylopectin (75−80%). The chemical structure of amylose contains α-D-glucose monosaccharides linked through α1 → 4 glycosidic bond, whereas amylopectin contains α-D-glucose monosaccharides linked through α1 → 4 glycosidic bond and branching takes place with α1 → 6 bonds occurring every 24−30 glucose units.
75. Chronakis, I. S. On the Molecular Characteristics, Compositional Properties and Structural Functional Mechanism of Maltodextrins. A Review. *Crit. Rev. Food Sci. Nutr.* **1998**, *38*, 599–637.
76. Lactose consists of β-D-galactose and β-D-glucose monosaccharides linked through β1→4 glycosidic bond.
77. Kikes, E. S. *Industrial Polymers Handbook*; Wiley-VCH: Weinheim, Germany, 2001; Vol. 3,4.
78. Auvray, X.; Petipas, C.; Anthore, R. X-ray Diffraction Study of the Ordered Lyotropic Phases Formed by Sugar-Based Surfactants. *Langmuir* **1995**, *11*, 433–439.
79. Ariga, K.; Vinu, A.; Hill, J. P.; Mori, T. Coordination Chemistry and Supramolecular Chemistry in Mesoporous Nanospace. *Coord. Chem. Rev.* **2007**, *251*, 2562–2591.
80. Corriu, R. J. P.; Mehdi, A.; Reyé, C. Molecular Chemistry and Nanosciences: On the Way to Interactive Materials. *J. Mater. Chem.* **2005**, *15*, 4285–4294.
81. Katz, E.; Willner, I. Integrated Nanoparticle-Biomolecule Hybrid Systems: Synthesis, Properties and Applications. *Angew. Chem., Int. Ed.* **2004**, *43*, 6042–6108.
82. Balaji, T.; El-Safty, S. A.; Matsunaga, H.; Hanaoka, T.; Mizukami, F. Optical Sensors on Nanostructured Cage Materials for the Detection of Toxic Metal Ions. *Angew. Chem., Int. Ed.* **2006**, *45*, 7202–7208.
83. El-Safty, S. A.; Ismail, A. A.; Matsunaga, H.; Mizukami, F. Optical Nanosensor Design with Uniform Pore Geometry and Large Particle Morphology. *Chem.—Eur. J.* **2007**, *13*, 9245–9255.
84. Slowing, I. I.; Trewyn, B. G.; Lin, V.S.-Y. Mesoporous Silica Nanoparticles for Intracellular Delivery of Membrane-Impermeable Proteins. *J. Am. Chem. Soc.* **2007**, *129*, 8845–8849.
85. Mortera, R.; Vivero-Escoto, J.; Slowing, I. I.; Garrone, E.; Onidaa, B.; Lin, V.S.-Y. Cell-Induced Intracellular Controlled Release of Membrane Impermeable Cysteine from a Mesoporous Silica Nanoparticle-Based Drug Delivery System. *Chem. Commun.* **2009**, 3219–3221.
86. Zhao, Y.; Trewyn, B. G.; Slowing, I. I.; Lin, V.S.-Y. Mesoporous Silica Nanoparticle-Based Double Drug Delivery System for Glucose-Responsive Controlled Release of Insulin and Cyclic AMP. *J. Am. Chem. Soc.* **2009**, *131*, 8398–8400.
87. Rosenholm, J. M.; Meinander, A.; Peuhu, E.; Niemi, R.; Eriksson, J. E.; Sahlgren, C.; Linden, M. Targeting of Porous Hybrid Silica Nanoparticles to Cancer Cells. *ACS Nano* **2009**, *3*, 197–206.
88. Xia, T.; Kovochich, M.; Liong, M.; Meng, H.; Kabehie, S.; George, S.; Zink, J. I.; Nel, A. E. Polyethyleneimine Coating Enhances the Cellular Uptake of Mesoporous Silica Nanoparticles and Allows Safe Delivery of siRNA and DNA Constructs. *ACS Nano* **2009**, *3*, 3273–3286.
89. Rosenholm, J. M.; Peuhu, E.; Eriksson, J. E.; Sahlgren, C.; Lindén, M. Targeted Intracellular Delivery of Hydrophobic Agents Using Mesoporous Hybrid Silica Nanoparticles as Carrier Systems. *Nano Lett.* **2009**, *9*, 3308–3311.
90. Warburg, O. On the Origin of Cancer Cells. *Science* **1956**, *123*, 309–314.
91. Christofk, H. R.; Vander Heiden, M. G.; Harris, M. H.; Ramanathan, A.; Gerszten, R. E.; Wei, R.; Fleming, M. D.; Schreiber, S. L.; Cantley, L. C. The M2 Splice Isoform of Pyruvate Kinase Is Important for Cancer Metabolism and Tumor Growth. *Nature* **2009**, *452*, 230–233.
92. Hillaireau, H.; Couvreur, P. Nanocarriers' Entry into the Cell: Relevance to Drug Delivery. *Cell. Mol. Life Sci.* **2009**, *66*, 2873–2893.
93. Lu, J.; Liong, M.; Sherman, S.; Xia, T.; Kovovich, M.; Nel, A. E.; Zink, J. I.; Tamanoi, F. Mesoporous Silica Nanoparticles for Cancer Therapy: Energy-Dependent Cellular Uptake and Delivery of Paclitaxel to Cancer Cells. *Nanobiotechnology* **2007**, *3*, 89–95.
94. Gemeinhart, R. A.; Luo, D.; Saltzman, W. M. Cellular Fate of a Modular DNA Delivery System Mediated by Silica Nanoparticles. *Biotechnol. Prog.* **2005**, *21*, 532–537.
95. Klionsky, D. J.; Abeliovich, H.; Agostinis, P.; Agrawal, D. K.; Aliev, G.; Askew, D. S.; Baba, M.; Baehrecke, E. H.; Bahr, B. A.; Ballabio, A.; *et al*. Guidelines for the Use and Interpretation of Assays for Monitoring Autophagy in Higher Eukaryotes. *Autophagy* **2007**, *4*, 151–175.
96. Formari, F. A.; Randolph, J. K.; Yalowich, J. C.; Ritke, M. K.; Gewirtz, D. A. Interference by Doxorubicin with DNA Unwinding in MCF-7 Breast Tumor Cells. *Mol. Pharmacol.* **1994**, *45*, 649–656.
97. Patil, R. R.; Guhagarkar, S. A.; Devarajan, P. V. Engineered Nanocarriers of Doxorubicin: A Current Update. *Crit. Rev. Ther. Drug Carrier Syst.* **2008**, *25*, 1–61.
98. Fisichella, M.; Dabboue, H.; Bhattacharyya, S.; Saboungi, M. L.; Salvetat, J. P.; Hevor, T.; Guerin, M. Mesoporous Silica Nanoparticles Enhance MTT Formazan Exocytosis in HeLa Cells and Astrocytes. *Tox. Vitro* **2009**, *23*, 697–703.